Structural Switching in Tetrathiafulvalene based Metal-Organic Frameworks

Nathan Jake Corr

A thesis submitted in fulfilment of the requirements
for the degree
Master of Philosophy (Science)

School of Chemistry
The University of Sydney
30 June 2024

Statement of Originality

This is to certify that to the best of my knowledge, the content of this thesis is my own work. This thesis has not been submitted for any degree or other purposes.

I certify that the intellectual content of this thesis is the product of my own work and that all the assistance received in preparing this thesis and sources have been acknowledged.

Nathan Jake Corr

Abstract

Due to their high tuneability, Metal-Organic Frameworks (MOFs) are being investigated for incorporation into high performance switching materials. Switchable MOFs are able to combine their high tuneability with functionalised components, to create a wide array of switching behaviours. Understanding the behaviour and conditions required for switching to occur is a key step in developing switchable MOFs for applications. The rigidity and tuneability of MOFs provide the ability to precisely investigate these properties. This thesis investigates a structural transition occurring in a series of MOFs that contain 2,6-*Bis*(4-pyridyl)-tetrathiafulvalene (Py_2TTF), one of which occurs outside of the known criteria.

The ability for $[Cd_2(bpdc)_2(Py_2TTF)_2]$ (bpdc = 1,4 biphenyldicarboxylate) to undergo a double [2+2] photo-induced cycloaddition between the TTF cores when exposed to white light inspired further investigation into its analogues. One of these frameworks, $[Zn_2(TDC)_2(Py_2TTF)_2]$ (Zn-C) (TDC = 2,5-thiophenedicarboxylate) was observed to undergo a photo-induced structural change, but contained crossed TTF ligands, that were far outside the known Schmidt criteria for photocycloaddition. This photo-induced structural change caused significant crystal cracking, preventing the determination of the resulting structure.

Chapter **3** discusses a series of optimisations of the synthetic conditions forming $[Zn_2(TDC)_2(Py_2TTF)_2]$. A novel framework $[Zn_2(TDC)_2(Py_2TTF)]$ (Zn-Pad) was found to form alongside $[Zn_2(TDC)_2(Py_2TTF)_2]$. These optimisations served to to reduce the formation of Zn-Pad, and to reduce the extreme crystal cracking that had previously prevented structural characterisation of the product of the double [2+2] photo-induced cycloaddition (Zn-Cyc). Zn-Cyc was found to contain disordered $Py_4C_{12}S_8H_4$ produced by the photocyclisation. Due to the crossed nature of the Py_2TTF dimers in Zn-C, one of the ligands within each dimer must undergo significant molecular motion to form Zn-Cyc.

Chapter **4** reports the synthesis of a novel Cd-Analogue of Zn-C, $[Cd_2(TDC)_2(Py_2TTF)_2]$ (Cd-C). This framework was found to undergo a reversible photo-induced structural transition. Solid-state UV-Vis spectroscopy, Raman spectroscopy and cyclic voltammetry demonstrated the presence of Py_2TTF and the formation of $Py_4C_{12}S_8H_4$.

A Raman spectroscopy based kinetic study of the photo-induced transitions in Zn-C and Cd-C was undertaken, modelling kinetic results with the Johnson, Mehl, Avrami, and Kolmogorov (JMAK) model and the Finke-Watzky autocatalytic and autoinhibitive models. This study develops considerations to modelling kinetics to account for ambient light exposure, through the development of a modified Finke-Watzky (FW) kinetic model and a normalisation method.

Through JMAK modelling, Zn-C was found to have a reaction rate (k) of 0.62 ± 0.17 and an Avrami constant (n) of 2.03 ± 0.78. The FW modelling finds a reaction rate (k_1) of 0.027 ± 0.006 and an autocatalysed reaction rate (k_2) of 0.007 ± 0.007, with the Autoinhibitive model finding a reaction rate (k_1) of 0.040 ± 0.017 and an autoinhibitive reaction rate (k_2) of -0.012 ± 0.016. Each of these models agree that no autocatalytic or autoinhibitive effects are present within the photocycloaddition of Zn-C.

Cd-C, through JMAK modelling, was found to have a reaction rate (k) of 0.38 ± 0.14 and an

Avrami constant (n) of 0.98 ± 0.27. The FW modelling finds a reaction rate (k_1) of 0.026 ± 0.005 and an autocatalysed reaction rate (k_2) of 0, with the Autoinhibitive model finding a reaction rate (k_1) of 0.062 ± 0.010 and an autoinhibitive reaction rate (k_2) of -0.060 ± 0.026. Each of these models agree that an autoinhibitive effect takes place during the photocycloaddition of Cd-C.

These kinetic results show a unique kinetic behaviour of Zn-C that is attributed to the crossed Py_2TTF ligands. The photo-induced structural change within Cd-C is analogous to previously reported behaviours of $[Cd_2(bpdc)_2(Py_2TTF)_2]$.

Acknowledgements

This research reported in this thesis was supported by the award of a Research Training Program scholarship.

I would like to thank my supervisor Professor Deanna D'Alessandro for the continuous advice and encouragement across the past two years. I have continued to become a better chemist through your expertise.

The Molecular Materials Group has been a pleasure to be in. The brainteasers and geography games have improved many days of data processing and synthesis. I would like to thank Dr Eleanor Kearns for the technical advice and assistance throughout my Masters. I truly appreciate the time you have spent answering my many questions. Dr Marcello Solomon has provided editing feedback throughout the many drafts of my thesis. The thoroughness of your feedback has improved my work much more than it would have otherwise.

To Dr Michelle Wood, Dr William Lewis, Dr Sam Duyker, thank you for your technical assistance in making my experiments possible. I appreciate the ability to learn about a varied range of techniques.

On a personal note, this wouldn't have been possible without the amazing support from my family. You have all made the long days more bearable, and the short days excellent. To my partner Kawana, I am grateful for the many lunches that we have shared during this time. Thank you for always making time to listen to me talk.

Table of Contents

List of Figures

List of Tables

List of Abbreviations

Py_2TTF 2,6-*Bis*(4-pyridyl)-tetrathiafulvalene

4-nvp 4-(1-naphthylvinyl)pyridine

4spy 4-styrylpyridine

ANOVA Analysis of Variance

BDC 1,4 benzenedicarboxylate

BIO (*E*)−2-(2,4−dichlorobenzylidene)−2,3−dihydro−1H−in−den−1-one

BPDC 1,4 biphenyldicarboxylate

bpe *trans*−1,2−bis(4-pyridyl)ethylene

bpeb ce1,4-bis[2-(4-pyridyl) ethenyl]benzene

CCDC Cambridge Crystallographic Data Centre

Cd-C $[Cd_2(TDC)_2(Py_2TTF)_2]$

Cd-Cyc $[Cd_2(TDC)_2(Py_4C_{12}S_8H_4)]$

cin cinnamate

CP Coordination Polymer

CV cyclic voltammogram

D-cam D-camphoric acid

DCM dichloromethane

DMF N,N'-dimethylformamide

DoE Design of Experiments

EtOH ethanol

FW Finke-Watzky

FWHM full width at half maximum

H4ohbz 4-hydroxy benzoic acid

hfp 4,4'−(hexafluoroisopropylidene)bis(benzoate)

HOMO highest occupied molecular orbital

JMAK Johnson, Mehl, Avrami, and Kolmogorov

LUMO lowest unoccupied molecular orbital

MOF Metal-Organic Framework

NMR Nuclear Magnetic Resonance

PS Photosalient

PXRD Powder X-Ray Diffraction

SBU Secondary Building Unit

SC-SC single-crystal-to-single-crystal

SCXRD Single Crystal X-Ray Diffraction

stil 4,4-stilbenedicarboxylic acid

TDC 2,5-thiophenedicarboxylate

TFMS trifluoromethane sulphonic acid

TGA Thermogravimetric Analysis

TPDC 1,4 terphenyldicarboxylate

TTF tetrathiafulvlene

TTFTB tetrathiafulvalene tetrabenzoate

Zn-C $[Zn_2(TDC)_2(Py_2TTF)_2]$

Zn-Cyc $[Zn_2(TDC)_2(Py_4C_{12}S_8H_4)]$

Zn-Pad $[Zn_2(TDC)_2(Py_2TTF)]$

Å Angstrom

Chapter 1. Introduction

1.1 Coordination Polymers

Coordination Polymers (CPs) are compounds consisting of metal ions or clusters linked by organic ligands that extend continuously in 1, 2 or 3-dimensions, through coordination bonds.[1] The topology of the resulting CP is determined by the coordination sphere of the metal ion, and the denticity of the linking organic ligands, as metal ions or metal ion based polynuclear clusters, which act as nodes, and are connected by ligands (Figure 1.1).

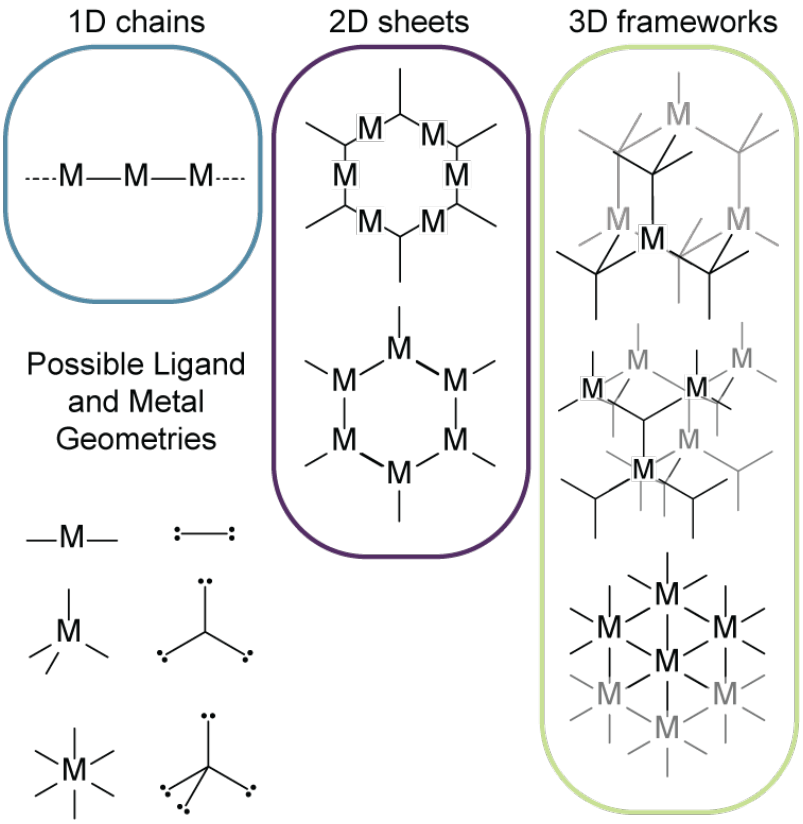

Figure 1.1: The impact of metal ion coordination spheres and denticity of ligands on lattice dimensionality.

Historically, the utilisation of pore spaces within CPs was limited by the weak and non-directional nitrile and pyridyl based bonds which connected the metal ions and the neutral organic ligands. These weak and non-directional bonds resulted in framework collapse when pore solvents were removed.[2–4]

Hoskins and Robsons work, 'Infinite Polymeric Frameworks Consisting of Three Dimensionally Linked Rod-like Segments'[5] proposed a class of CPs. By linking together tetrahedral metal centres with rod-like ligands they were able to form an infinite lattice with regular voids. The establishment of permanent porosity within these frameworks lead to the development of

Metal-Organic Frameworks (MOFs).

1.2 Metal-Organic Frameworks

Metal-organic frameworks (MOFs) are a class of coordination polymers comprised of metal ions linked in 1, 2 or 3-dimensions by organic ligands with potential voids.[1] MOFs exhibit permanent porosity[1] and typically have high internal surface areas.[6]

Due to their high surface areas, MOFs are promising for use in gas storage[7,8] and separations.[9] The highly tuneable structure of MOFs allows them to be designed and used for applications in sensing[10,11] and catalysis.[12,13] The potential applications of MOFs can be expanded through variations in ligand geometry,[14–16] the coordination sphere of the metal ion,[15–17] and the incorporation of functional groups.[13,18,19] Through these modifications MOFs can be tuned to create a wide array of specialised materials.

In 1998, Yaghi *et al.* developed MOF-2 with the formula $Zn(BDC)\cdot(DMF)(H_2O)$, where BDC = 1,4 benzenedicarboxylate and DMF = N,N'-dimethylformamide. MOF-2 was able to withstand the removal of pore solvent, a process called framework activation. The BDC ligands formed strong directional bonds with the Zn^{II} metal centres which provided enough stability for the framework to withstand activation (Figure 1.2).[20] Switching from flexible ligands with weak binding groups, present in the nitrile and pyridyl CPs, to rigid ligands with stronger, directional binding groups, such as carboxylic acids, allowed MOFs to withstand solvent loss.

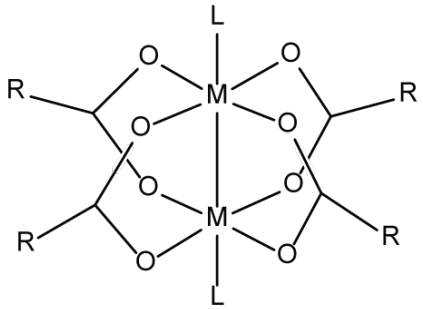

Figure 1.2: A paddlewheel SBU

The strong directional bonds used within MOFs lead to the formation of predictable polynuclear structural units, called Secondary Building Units (SBUs), throughout the framework.[4,21] The assembly of secondary building structure around the metal ion can allow for topologies to be defined by the connectivity of the SBU rather than the coordination sphere of the metal ion.

The SBU approach increases the ways in which MOFs can be tuned for applications. The IRMOF series was tuned for methane sorption, through the use of a varied series of ligands.[22,23] The resulting MOFs were all topologically identical due to the zinc acetate SBU. The various ligands used resulted in a tuned methane uptake of 240 cm^3 in IRMOF-6 compared to 135 and 120 cm^3 in IRMOF-1 and IRMOF-3 respectively.

By maintaining the geometry of the SBU, ligands and metals within the framework can be substituted while the overall MOF's topological structure remains the same, creating isostructural series'.[4] Through the creation and investigation of isostructural series', the effects of different ligands and metals on a framework topology can be studied.

An example of the formation of an isostructural series is the UIO-66/67/68 series,[24] which uses BDC, 1,4 biphenyldicarboxylate (BPDC) and 1,4 terphenyldicarboxylate (TPDC) as organic ligands respectively. UIO-66 was calculated to have an internal surface area of 1187 m^2/g, while UIO-67 and 68 had internal surface areas of 3000 and 4170 m^2/g respectively.[25] This forms a series that has the same topology, but increasing internal surface area as the ligand length extends.

1.3 [2+2] Photocycloadditions within Metal Organic Frameworks

1.3.1 Stimuli Responsive Materials

Multifunctional materials, or smart materials, are able to respond to stimuli with functional behaviours.[26] Through combining multiple stimuli responsive behaviours within the same material, new multifunctional materials can be created and tuned to a variety of applications. The incorporation of stimuli responsive switches,[27] which undergo a reversible transformation between two states, enable these multifunctional materials to be regenerated for further use. Switchable materials require stability over multiple cycles.[28,29]

Light,[30–32] temperature,[33,34] pressure,[35] magnetic,[36] and electrical[37] stimuli have all been used to create switchable behaviours. Light, particularly wavelengths near and within the visible spectrum, are advantageous as a switching stimulus, as stimuli responsive materials can be remotely activated, and switching responses can occur through sunlight[38]

1.3.2 Stimuli Response within MOFs

MOFs are great candidates for designing switchable and multifunctional materials.[27] MOFs are able to respond to external stimuli through single-crystal-to-single-crystal (SC-SC) transitions,[39,40] exchange of guest molecules[30,41] and alterations in adsorption of guest molecules,[42] as well as through the inclusion of functional responses like conductivity,[35] redox activity,[39] spin crossover[31,43] and chiral response.[44]

The stimuli detection and response can be altered through tuning of MOF topology,[34,45] appending functional groups through post synthetic modification[40] and incorporating functional responses of guest molecules,[41,46] metal sites[31] and organic ligands.[30,32,39,42]

Switching within MOFs can be monitored through crystallographic or spectroscopic techniques to further understand the mechanisms that drive switchable property changes. One light induced switchable reaction is the [2+2] photocycloaddition, which has been utilised by Vittal *et al.* to create dimensionality change.[47,48]

1.3.3 [2+2] Photocycloaddition

A [2+2] photocycloaddition involves the reaction of two olefins, one of which needs to be excited by UV or visible light, forming a carbocyclic product.[49] The reaction can occur *via* the First Excited Singlet State pathway or the First Excited Triplet State pathway.

The First Excited Singlet State pathway involves the excitation of one olefin from its ground state S_0 to excited state S_1 and its subsequent addition to another olefin (Figure 1.3).[49]

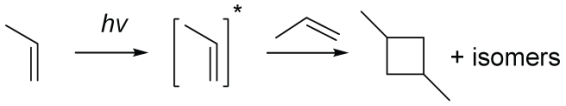

Figure 1.3: [2+2] Photocycloaddition *via* its First Excited Singlet State

When the reaction occurs through the First Excited Triplet State, intersystem crossing occurs from the excited singlet state S_1 to the lowest lying triplet state T_1, which is often $\pi\pi^*$ in character (Figure 1.4).[49] A second intersystem crossing then enables the product to be formed.

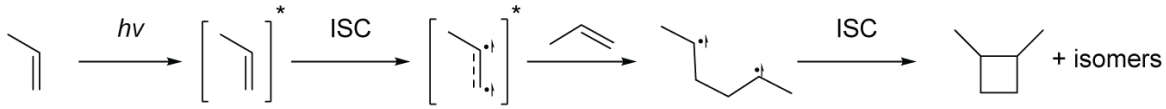

Figure 1.4: [2+2] Photocycloaddition *via* its First Excited Triplet State

The First Excited Triplet State mechanism has a long lived radical and a higher energy demand, compared to the First Excited Singlet State. This difference in behaviour between the two pathways is prominent in solution state photocycloadditions, when compared to solid state photocycloadditions. Solution state photocycloaddition pathways require long lived excitation times to provide time for contact with another olefin. Solid state photocyclisations can occur more easily as the crystalline lattice holds reacting groups in relative proximity to each other.

1.3.3.1 Schmidt's rule and geometric considerations for photocyclisations in the solid state

Solid state photocycloadditions only occur under very strict conditions due to the rigidity and regularity of crystalline networks. The types of solid state photocycloadditions achievable are generally defined by Hertel's topochemical factors.[50,51] Schmidt outlined the controlling factors of solids state reactions, building from the concept that reactions in the solid state occur with a minimal amount of atomic or molecular movement.[51]

The geometric conditions for [2+2] photo-induced cycloadditions in the solid state were well studied by Schmidt in cinnamic acids in 1964.[52] Through the study of a series of *cis*-cinnamic acids, four approximate criteria were defined by Schmidt: the distance between the olefin carbons must be between 3.5 and 4.2 Å, and three key angles between the bond pairs, relative

rotation (θ_1) and skew (θ_2), which should both approach 0° and relative offset θ_3, which should approach 90°, (Figure 1.5).

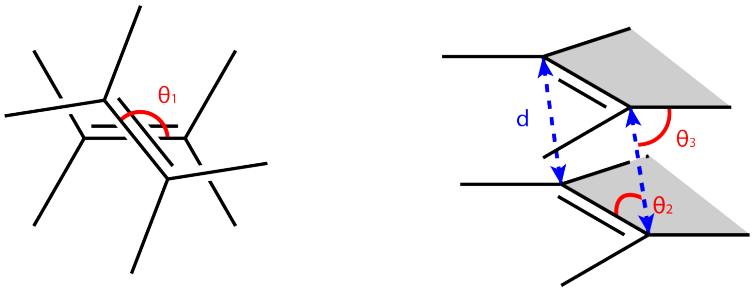

Figure 1.5: The geometric criteria that effect a [2+2] cycloaddition between olefins. (d = distance between the olefin pairs, θ_1 = relative rotation, θ_2 = skew, θ_3 = relative offset)

The Schmidt criteria are not conclusive as to whether or not a [2+2] photocycloaddition will occur. One such structure, 7-chlorocoumarin[53] has a packing arrangement such that two pairs of potentially reactive olefins are brought together. A translationally related pair has a centre to centre distance of 4.54 Å, which if photocyclised would yield a head-head dimer, while the centrosymmetrically related pair has a centre to centre distance of 4.12 Å which if photocyclised would yield a head-tail dimer. Applying the Schmidt criteria would indicate that the centrosymmetrically related pair should photocyclise, while the translationally related pair should not. When 7-chlorocoumarin was irradiated, the head-head dimer was obtained at 70% yield. This was due to the relative high lattice energy of the ideal crystal geometry of the centrosymmetrically related pair, compared to the translationally related pair.

It has been suggested that the surrounding electron environment may restrict the ability for a [2+2] photocycloaddition to occur.[54] For example, (*E*)−2-(2,4−dichlorobenzylidene)−2,3−dihydro−1H−in−den−1-one (BIO) crystallised into 1-dimensional columns ordered by $\pi-\pi$ stacking, bringing C=C bonds into a head to head packing arrangement, with a bond separation of 3.84 Å and a θ_1 angle of 117.3°. Despite meeting the Schmidt criteria, BIO does not photocyclise, which is attributed to $C{=}O\cdots H(CH_2)$ interactions between molecules confining the reactive bond pair.[54] A relatively small HOMO-LUMO gap may be required between the π orbitals of the alkene for the reaction to occur.[55]

1.3.3.2 [2+2] Cycloaddition outside of Schmidt criteria

[2+2] Photo-induced cycloadditions occur outside of the Schmidt criteria as well.[56–59] Vittal *et al.* reported $[Zn_2(cin)_4(4spy)_2]$ (cin = cinnamate and 4spy = 4-styrylpyridine) which undergoes a double [2+2] photo-induced cycloaddition, despite the reactive olefins being separated by 4.348(2) Å.[60]

Some [2+2] photo-induced cycloaddition reactions that are thought to occur out of the Schmidt criteria are instead brought within the required parameters through thermal motion or energetically unfavourable structural transformations.[53,61,62] It is also possible that

photoexcitation may change the geometry and polarizability of the reacting olefins such that the geometric conditions of the ground state cannot predict the outcome. Crystals of 7-methocoumarin were found to undergo a photocycloaddition, yet their photoreactive dimers are at a θ_1 angle of 67.5°. far outside the Schmidt Criteria (Figure 1.5).[53]

An organic salt [bpeH]·TFMS (bpe = *trans*−1,2−bis(4-pyridyl)ethylene, TFMS = trifluoromethane sulphonic acid) contained C=C double bonds at a distance of 4.97 Å, with the bonds in an antiparellel orientation.[62] It was observed to undergo [2+2] photocyclisation when exposed to UV irradiation for 13 hours. [bpeH]·TFMS was determined through ^1H NMR to undergo a pedal like motion through the bpe, bringing the C-C double bonds into a parallel orientation, in order to photocyclise.

Understanding the molecular movement within solid state systems which fall outside of the Schmidt criteria are key to predicting whether [2+2] photocycloadditions will occur.

1.3.3.3 Solid state kinetics of [2+2] photocycloadditions

In order to effectively incorporate [2+2] photocycloadditions into multifunctional materials and devices, it is important to be able to quantify the rate at which these reactions occur and determine ways to model [2+2] photocycloadditions in the solid state.

Within solid state materials, reactions change their surrounding chemical environment, which may promote or inhibit the surrounding reactive sites. These changes may propagate cooperatively throughout the crystal lattice, causing an autocatalytic, or autoinhibitive effect in the reaction rate observed. Solution state kinetics cannot be applied accurately to these materials, as these models account for random collisions, and cannot account for cooperative effects.

The two main kinetic models used for solid state [2+2] photocycloadditions are the Johnson, Mehl, Avrami, and Kolmogorov (JMAK) model and the Finke-Watzky (FW) model.

The JMAK kinetic model was initially used to describe a two stage (nucleation and growth) phase change in metallurgy.[63–66] The kinetic model has since been applied to other sigmoidal based reactions including solid state photocyclisations.[67]

$$y = 1 - e^{(-kt^n)} \tag{1.1}$$

In the generic form of the JMAK equation (Equation 1.1), y represents the proportion of phase transformation that has occurred, k is the rate constant, t is time and n is the Avrami constant.

The Avrami constant represents the "dimensionality" of the crystal growth, with a constant of n representing n-1 dimensional growth, with the case of n=1 interpreted as a homogeneous, randomly occurring reaction. Non integer Avrami constants in solid state [2+2] photocycloadditions have generally been interpreted as a combination of a lower dimensionality of growth, coupled with an autocatalytic effect, or a higher dimensionality of growth, coupled with an autoinhibitive effect.

For example, in the photocyclisation of α-*trans*-Cinnamic Acid to α-Truxillic Acid,[68] an Avrami constant of 1.43 ± 0.08 was observed. Single Crystal X-Ray Diffraction (SCXRD) on pairs

of *α-trans*-Cinnamic Acid in undimerized and 79% converted samples showed that as the reaction proceeded the θ_3 angle was brought from 18.4° away from ideal to 10.9°. This was proposed to increase the likelihood of reaction between reaction pairs, creating an autocatalytic effect, with a homogeneous reaction.

Similarly, a sulfonic substitution of *α-trans*-Cinnamic Acid, p-sulfocinnamic acid was found to have a Avrami constant of 1.8(1).[69] In this instance the reaction was said to proceed with 1-dimensional linear growth (n=2), with a decreasing nucleation rate, causing an autoinhibitive effect as the reaction continued.

JMAK modelling has been used to study an array of different photocycloadditions including the [4 + 4] photodimerization of 1,4-dimethyl-2-pyridinone,[70] 9-methylanthracene.[71]

Within the generic form of the JMAK equation, k and n are mutually dependant, so a linearised form of the equation is used in modelling experimental data (Equation 1.2).[72,73]

$$\ln(\ln(1/y)) = \ln(k) + n\ln(t) \tag{1.2}$$

The Finke-Watzky model is another cooperative sigmoidal growth model,[74] that seeks to provide physical model-based parameters. It was originally derived to model the nucleation and growth of nanoparticles, but has since been applied to model other systems exhibiting nucleation and growth behaviours, including protein aggregation and solid state reactions.[75–77] The model includes a first order reaction step (Equation 1.3) and a fast autocatalytic step (Equation 1.4).

$$A \xrightarrow{k_1} B \tag{1.3}$$

$$A + B \xrightarrow{k_2} 2B \tag{1.4}$$

$$-\frac{d[A]}{dt} = \frac{d[B]}{dt} = k_1[A] + k_2[A][B] \tag{1.5}$$

$$\alpha = \frac{k_1 + k_2}{k_2 + k_1 e^{(k_1+k_2)t}} \tag{1.6}$$

This models the reaction proceeding from $A \rightarrow B$ with a reaction rate k_1 and an autocatalysed reaction rate k_2, where t = time. This rate law can then be integrated, relying on the assumption $k_1 \ll k_2[A]_0$,[75,78] to give Equation 1.6 where α = the fraction of phase transformation.

Since the FW model can only account for autocatalytic effects, Kohout proposed an Autocatalytic model, in which sign flipping of Equation 1.6 turns k_2 from an autocatalytic rate constant, to an autoinhibitive one.[79]

A 2009 meta-study compared the JMAK and FW models, across a series of 12 solid state reactions.[80] Across the set of 12 reactions JMAK fit better for three, FW fit better for two, and neither model was statistically preferred in the other 7. Since both models found similarly good fits for the majority of tested cases, the authors compared both models to see if they were mathematically equivalent. Preliminary results indicate that the reaction rate and Avrami constants of the JMAK model may be dependant on the k_1 and k_2 of the FW model.

1.3.4 [2+2] Cycloaddition with MOFs

The rigidity and ordering within MOFs provide the ability to probe the conditions for [2+2] photo-induced cycloaddition with high accuracy. [Zn(hfp)(4-spy)] (hfp = 4,4'−(hexafluoroisopropylidene)bis(benzoate)) was observed to photocyclise using UV light with an olefin to olefin distance of 5.9 Å. The ability to photocyclise for [Zn(hfp)(4-spy)] was attributed to thermal motion and isomerisation of the 4-spy ligands, which brought the pair of C-C double bonds significantly closer to each other.[81]

Within MOFs, [2+2] photo-induced cycloadditions have been found to be reversible using heat or light as the reversing stimuli.[82–84] This mechanism is especially useful within a switching material, as it allows for multiple stimuli to control changes, and for many response cycles to occur.

The incorporation of groups capable of undergoing [2+2] photo-induced cycloaddition within MOFs has been used to create materials with alterable electrical conductivity,[38] gas sorption,[85] molecular sensing[86] and photoactuation properties.[87]

A SC-SC transition involves the reaction of a single crystal such that the long range order and structure of the crystal lattice is undamaged.[88] These transitions provide the ability to observe mechanistic details of reactions as they unfold.[89]

Selugi *et al.* synthesised the framework $Zn_2(bpeb)_2(D-cam)_2$ (bpeb = ce1,4-bis[2-(4-pyridyl) ethenyl]benzene, D-cam = D-camphoric acid), which was capable of undergoing a double [2+2] photocycloaddition, when desolvated.[90] However, single crystalinity was lost during the desolvation process, and light irradiation produced significant crystal cracking, meaning the crystal structure of the photoproduct was unable to be obtained.

Some photoactive MOFs exhibit a variety of Photosalient (PS) effects during their reaction involving cracking, curling, jumping and rolling upon stimuli activation.[91,92] [2+2] Cycloadditions have been observed to induce many kinds of PS effects.[91,93] PS effects often result in cracking, preventing the study of the result of a solid state stimuli active transition, as the remaining crystal sizes are too small for SCXRD.[91] Additionally, materials exhibiting this cracking are not suitable for use as switchable materials across multiple cycles. Stress, induced by the formation of grain boundaries due to unit cell size change is thought to be the main contributor to PS effects.[94]

The metal ion in MOFs has been shown to play a role in facilitating PS effects. Khan *et al.* reported that the isostructural MOFs $[Zn(4\text{-ohbz})_2(4\text{-nvp})_2]$ and $[Cd(4\text{-ohbz})_2(4\text{-nvp})_2]$ (H4ohbz = 4-hydroxy benzoic acid (H4ohbz); 4-nvp = 4-(1-naphthylvinyl)pyridine (4-nvp)) undergo [2+2] photocycloaddition. The Zn-based framework exhibits PS behaviour, including jumping, splitting, rolling and swelling, while the Cd-based framework shows no PS behaviour.[93]

SCXRD is an extremely powerful technique for understanding the structural changes within crystalline materials. The photocyclisation process can introduce stress-induced cracking, removing the ability to obtain crystal structures of the resulting material. Finding methods to create SC-SC transitions within photoactive materials is vital for further structural understanding.

1.4 Tetrathiafulvalene (TTF)

Tetrathiafulvlene (TTF) has been widely studied for its electronic, structural and photochromic properties, for applications in charge transfer, semiconductors, and the creation of switchable materials.[95] TTF undergoes two reversible $1e^-$ oxidation processes, first to the cation radical and then to the dication at $E_{1/2}$ 1=0.37 V and $E_{1/2}$ 2=0.67 V vs Ag/AgCl in acetonitrile respectively (Figure 1.6).[95]

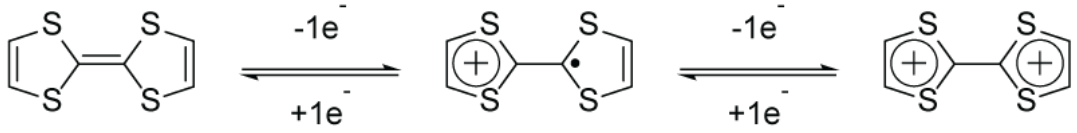

Figure 1.6: Redox Activity of TTF

TTF is a non-aromatic 14π electron molecule. Oxidation of TTF to $TTF^{\bullet+}$ or TTF^{2+} establishes aromatictiy in one or two of the 1,3-dithiolium rings respectively. This oxidation also forces a shape change within the TTF moiety, from a boatlike conformation to each ring adopting a rigid planar shape, stabilising the aromaticity.[96]

1.4.1 Photocyclisations of TTF in solid state

The first photocyclistaion of a TTF derivative was observed by Neilands *et al.*[97] in the *cis* arrangements of (*Z*) 4,4'-dibutoxycarbonyl, (*Z*) 4,4'-dimethoxycarbonyl and (*Z*)methoxycarbonyl substituted TTF (Figure 1.7). The *trans* arrangement (*E*) 4,4'-dibutoxycarbonyltetrathiafulvalene did not undergo photocycloaddition, which was attributed to the arrangement of the crystal lattice. These photocycloadditions only proceeded in the solid state, and a double [2+2] photocycloaddition in (*Z*) 4,4'-dibutoxycarbonyltetrathiafulvalene was suspected to occur.

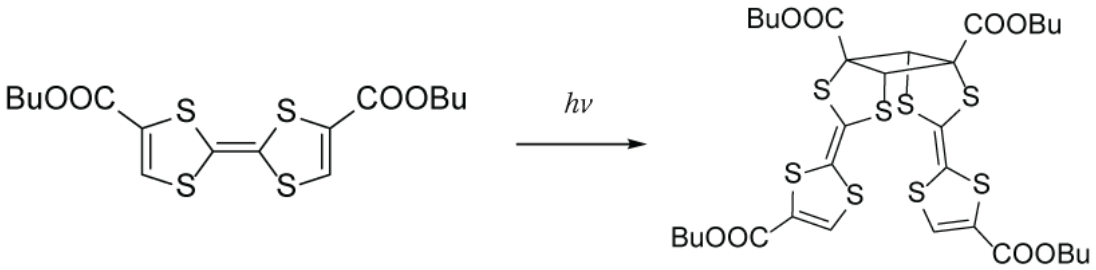

Figure 1.7: Photocyclisation of (Z) 4,4'-dibutoxycarbonyltetrathiafulvalene

Substituents on the TTF core influence the ability for TTF to photocyclise, through arrangements in crystal stacking[98] and creating a sufficiently small HOMO-LUMO gap, which seems to be required for [2+2] photo-induced cycloaddition to be promoted.[55]

The ability for TTF to transition between flat and boat geometries, through the establishment of aromaticity, impacts the photocyclisation of TTF. Jeannin and Fourmigué reported a CF_3-substituted TTF derivative that underwent a [2+2] photocycloaddition.[99] These crystallised into 1-D stacks with A-B-A-B ordering, where A had a bend in the TTF core of 8.36(8)°, while B was planar, causing racemic twinning, and significant loss of crystallinity during photocycloaddition.

Many of the TTF [2+2] photo-induced cycloaddditions that occur in the solid state involve only one of the two photoactive cites undergoing photocycloaddition, as one of the photoactive cites is substituted to attach to an electron-withdrawing group to promote photocycloaddition, and the other is attached to a group promoting $\pi - \pi$ interactions.[100,101] Out of the crystal structures of single [2+2] photocycloaddition in TTF found in the Cambridge Crystallographic Data Centre (CCDC), olefin to olefin distances of the second photoactive site range between of 4.069 - 4.35 Å.

Simao *et al.*[101] performed a kinetic study using the JMAK model on a carboxylate TTF and a carboxylic acid TTF at varying excitation wavelengths. They formed the conclusion that the optical properties of the photoproduct play a role in the reaction kinetics, as one of the wavelengths used was absorbed by the photoproduct and thus had a lower rate of photocycloaddition.

1.4.2 TTF In MOFs

The incorporation of TTF within MOFs and CPs has been used to make a wide array of multifunctional materials.[18] These materials generally focus on the redox active properties of TTF to make sensing[102] and switchable materials,[103,104] or utilise the MOF structure to stabilise the $TTF^{\bullet+}$ for optoelectronices[105] and photothermal conversion.[106]

One conductive TTF containing MOF, Cd_2(TTFTB) (TTFTB = tetrathiafulvalene tetrabenzoate), discovered by Park *et al.* has a conductance of σ = 2.68 (± 0.53) $\times 10^{-4}$ S/cm, which is one of the highest amongst microporous MOFs.[107]

[In(Me_2NH_2)(TTFTB)] uses multiple properties of the TTF unit in redox dependant breathing behaviours.[96] Breathing behaviours are reverisble structural transformations that result in a relatively large variation in unit cell dimensions.[108] These MOFs posses a flexible TTFTB ligand, which is able to distort into a boat like conformer to uptake N_2. Initially the MOF has a low N_2 uptake, of 70 cm^3g^{-1}, but as the pressure increases to 0.05 bar a breathing behaviour occurs, increasing the N_2 uptake to 340 cm^3g^{-1}. This behaviour relies on the flexibility of the TTF ligand. By soaking the crystals in I_2, TTF was oxidised to $TTF^{\bullet+}$, inhibiting the breathing behaviour.

The design of MOFs can be used to fix pairs of TTF units such that their olefin groups are held within the structural and chemical environment in order to undergo a double [2+2] photo-induced cycloaddition.

1.4.3 Double [2+2] photo-induced cycloaddition within MOFs

D'Alessandro *et al.* synthesised the framework $[Cd_2(bpdc)_2(Py_2TTF)_2]$ which when exposed to a 25 W microscope lamp for 15 min underwent a double [2+2] photo-induced cycloaddition to form $[Cd_2(bpdc)_2(Py_4C_{12}S_8H_4)]$ (Figure 1.8).[38] This was the first thermally reversible double [2+2] photo-induced cycloaddition of TTF.

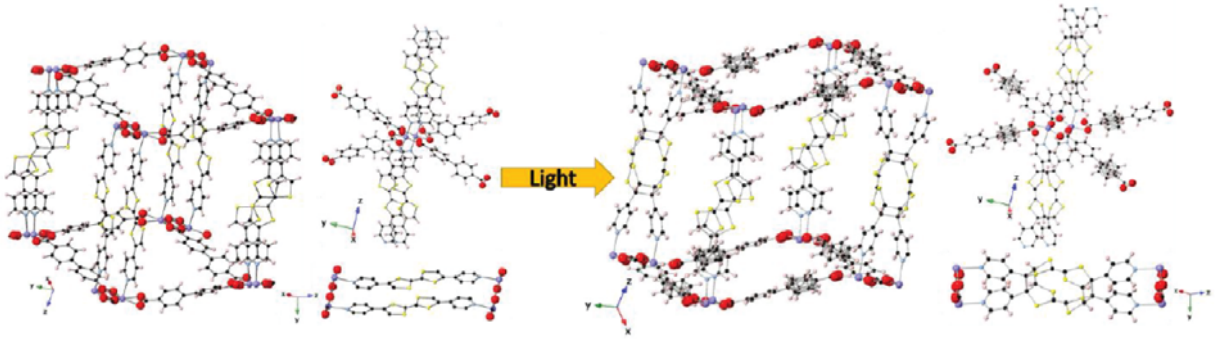

Figure 1.8: The double [2+2] photo-induced cycloaddition of $[Cd_2(bpdc)_2(Py_2TTF)_2]$ to form $[Cd_2(bpdc)_2(Py_4C_{12}S_8H_4)]$. Figure reprinted from Nature Communications under a Creative Commons License[38]

The $[Cd_2(bpdc)_2(Py_2TTF)_2]$ framework was able to reform when it was heated to 150 °C for 10 minutes. Since the $Py_4C_{12}S_8H_4$ dimer does not retain the characteristic electrochemical process of Py_2TTF, this material exhibits switchable redox activity through a reversible double [2+2] cycloaddition. A series of analogous MOFs have been synthesized, with many exhibiting the same double [2+2] photo-induced cycloaddition as $[Cd_2(bpdc)_2(Py_2TTF)_2]$.[109] These isostructural frameworks have utilised Zn instead of Cd, as well as varying the dicarboxylic acid used as a coligand (Figure 1.9).

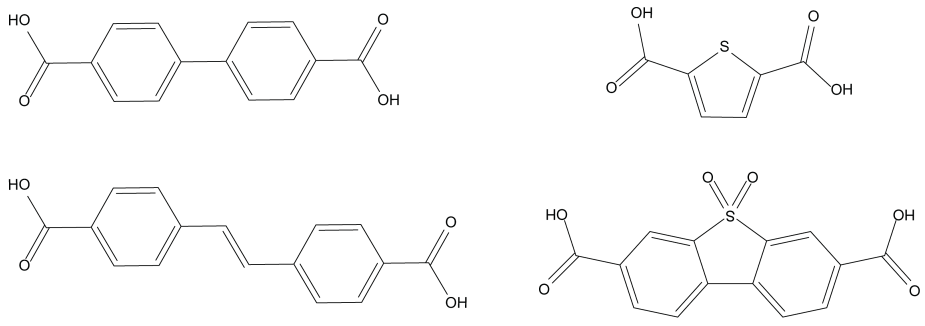

Figure 1.9: Coligands used in the isostructural series $[M_2(coligand)_2(Py_2TTF)_2]$

The kinetics of the solid state [2+2] photocycloaddition have been characterised for $[Cd_2(bpdc)_2(Py_2TTF)_2]$ and $[Cd_2(stil)_2(Py_2TTF)_2]$ (stil = 4,4′-stilbenedicarboxylic acid) at variable temperatures using both the JMAK and FW models.[109,110] The Avrami constant for $[Cd_2(bpdc)_2(Py_2TTF)_2]$ was shown to be 0.67 ± 0.08 at 20 °C and $[Cd_2(stil)_2(Py_2TTF)_2]$ was found

to have an Avrami constant of 0.77 ± 0.11 at 20 °C. Both Avrami constants were less than 1, indicating 0-dimensional growth with a degree of autoinhibition, which was attributed to increased strain induced in the crystals throughout the photocyclisation.

PS effects were observed in both $[Cd_2(bpdc)_2(Py_2TTF)_2]$ and $[Cd_2(stil)_2(Py_2TTF)_2]$, which exhibited cracking[110] and in the case of $[Cd_2(stil)_2(Py_2TTF)_2]$ jumping and curling.[109]

$[Zn_2(TDC)_2(Py_2TTF)_2]$ (TDC = 2,5−thiophenedicarboxylate) was found to react when exposed to light in a manner consistent with double [2+2] photo-induced cycloaddition.[111] This was unusual as SCXRD showed that olefins in the TTF units were far outside of the range of the Schmidt criteria, between 4.39 and 4.89 Å apart. Additionally, each pair of Py_2TTF ligands were rotationally offset from each other, about the central bond of the TTF unit (Figure 1.10).

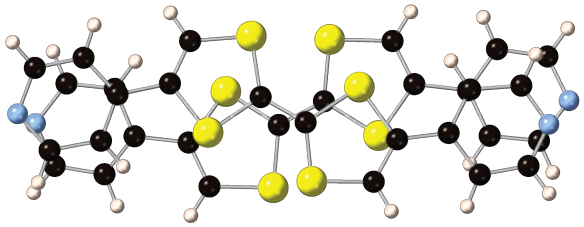

Figure 1.10: Rotational offset of the pairs of Py_2TTF units in $[Zn_2(TDC)_2(Py_2TTF)_2]$ from the SCXRD structure. Atom colours: H = White, C = Black, S = Yellow, N = Light blue

The product formed from irradiating $[Zn_2(TDC)_2(Py_2TTF)_2]$ could not be observed through SCXRD, as significant crystal cracking formed during the process. Significant molecular motion would be required in order to form the $Py_4C_{12}S_8H_4$ pillars present in the isostructural frameworks.

1.5 Project Aims

This project aims to investigate the properties of MOFs containing Py_2TTF ligands in cofacial arrangements. This project has two aims:

1. To further investigate the light induced structural change of $[Zn_2(TDC)_2(Py_2TTF)_2]$. This will involve efforts to improve single crystal size and stability to light induced change through improving the synthesis of $[Zn_2(TDC)_2(Py_2TTF)_2]$ in order to determine the structure formed after visible light irradiation.[111]

2. A Cd-based analogue of $[Zn_2(TDC)_2(Py_2TTF)_2]$ will be synthesised to compare the properties of Zn and Cd within the isostructural series. This will involve efforts to investigate the kinetics of photocyclisation of $[Zn_2(TDC)_2(Py_2TTF)_2]$ in comparison to $[Cd_2(TDC)_2(Py_2TTF)_2]$ through Raman spectroscopy.

Chapter 2. Methods

2.1 General Considerations

All reagents and solvents were commercially purchased and used without further purification unless otherwise stated. Dry toluene was obtained from a PureSolv MD solvent purification system.

2.2 Ligand Syntheses

Py_2TTF was synthesised according to modified literature processes.[38] One iteration of the synthesis of Py_2TTF was kindly performed by Dr Eleanor Kearns.

2.1.1 *4-(Bromoacetyl)pyridine hydrobromide.* Acetic acid (150 mL) and 4-acetyl pyridine (15 mL, 0.14 mol) were cooled to 0 °C. HBr (5 mL, 48%) was added and stirred for 10 min. Br_2/AcOH (1:1) 10 mL was added dropwise and the reaction mixture was stirred for 20 min at 0 °C and then for 25 min at room temperature. Excess Br_2 was removed by heating the reaction at 70 °C for 2 h. The precipitate was collected *via* vacuum filtration and washed with ethanol (EtOH) (2 × 30 mL) then diethyl ether (2 × 30 mL) to yield 4-(Bromoacetyl)pyridine hydrobromide as a white powder (4.55 g, 11.9% yield).

2.1.2 *Potassium isopropylxanthate.* KOH (22.0 g, 0.392 mol) was dissolved in isopropanol (250 mL) and cooled to 0 °C. Carbon disulfide (24 mL, 0.397 mol) was added dropwise and the reaction mixture was stirred for 30 min at 0 °C, before warming to room temperature. The mixture was filtered, washed with ethanol (EtOH) (3 × 50 mL), then recrystallised twice from ethanol (EtOH), obtaining Potassium isopropylxanthate as yellow needles (22.7 g, 33.2% yield).

2.1.3 *4-(4-Pyridyl)-1,3-dithiol-2-one.* 4-(Bromoacetyl) pyridine hydrobromide (8.26 g, 0.029 mmol) and potassium isopropylxanthate (5.42 g, 0.031 mol) were dissolved in H_2O (150 mL) and stirred for 1.5 h. The solution was then extracted with dichloromethane (DCM) (3 × 20 mL) and then H_2O (3 × 50 mL). The organic layer was dried with $MgSO_4$, filtered and the solvent removed *via* rotary evaporation, affording 4-(4-Pyridyl)-1,3-dithiol-2-one as a tan solid. ^{1}H NMR (300 MHz, $CDCl_3$) δ 7.17 (s, 1H), 7.32 (dd, J = 4.6, 1.7 Hz, 2H), 8.67 (dd, J = 4.6, 1.7 Hz, 2H).

2.1.4 *2,6-Bis(4-pyridyl)-tetrathiafulvalene* 4-(4-Pyridyl)-1,3-dithiol-2-one (2.36 g, 12.1 mmol) was added to a degassed solution of $P(OEt)_3$ (16 mL, 93.3 mmol) in dry toluene (16 mL) and heated at 110 °C under N_2 for 6 h under an inert atmosphere in the absence of light. The resulting solid was filtered and washed with MeOH (3 × 15 mL) then diethyl ether (2 × 15 mL), affording Py_2TTF as a red solid (1.26 g, 58.1%). ^{1}H NMR (300 MHz, D_{20}) δ 6.15 (s, 2H), 8.25 (d, J = 6.7 Hz, 4H), 8.80 (d, J = 6.7 Hz, 4H).

2.3 MOF Syntheses

All solvothermal MOF syntheses were performed in 21 mL glass scintillation vials and heated in a block heater at the heat and times specified.

For the synthesis of Zn-C two Full Factorial Design of Experiments (DoE) were implemented, varying the synthesis as per Table S.2 and S.1. The quality of the synthetic outcome was determined by the full width at half maximum (FWHM) of the 8.355° peak of the Powder X-Ray Diffraction Pattern, as well as through visual inspection of the yield outcome for crystal size, shape and uniformity.

[$Zn_2(TDC)_2(Py_2TTF)_2$] (Zn-C). $Zn(NO_3)_2 \cdot 6H_2O$ (5.4 mg, 0.018 mmol) was dissolved in EtOH (0.70 mL), H_2TDC (3.1 mg, 0.018 mmol) was dissolved in DMF (1.5 mL) and Py_2TTF (6.5 mg, 0.018 mmol) was dissolved in DMF (2.0 mL). The three solutions were combined, sealed and heated at 80 °C for 24 h in the absence of light. The resulting bright red, block-like crystals were purified by successive solvent washes with DMF, which was replaced until it remained colourless.

[$Zn_2(TDC)_2(Py_4C_{12}S_8H_4)$]$\cdot$2DMF (Zn-Cyc). Zn-TDC was irradiated with white light LEDs (4 W) for approximately 1 h to afford the cyclised framework, Zn-Cyc, as yellow/orange crystals.

[$Cd_2(TDC)_2(Py_2TTF)_2$] (Cd-TDC). $Cd(NO_3)_2 \cdot 4H_2O$ (5.5 mg, 0.018 mmol) was dissolved in EtOH (0.75 mL),H_2TDC (3.1 mg, 0.018 mmol) was dissolved in DMF (1.5 mL) and Py_2TTF (6.5 mg, 0.018 mmol) was dissolved in DMF (2.0 mL). The three solutions were combined, sealed and heated at 80 °C for 24 h in the absence of light. The resulting bright red, block-like crystals were purified by successive solvent washes with DMF, which was replaced until it remained colourless.

[$Cd_2(TDC)_2(Py_4C_{12}S_8H_4)$] (Cd-Cyc). Cd-TDC was irradiated with white light LEDs (4 W) for approximately 1 h to afford the cyclised framework, Cd-Cyc as yellow crystals.

2.4 Characterisation Techniques

Nuclear Magnetic Resonance (NMR)
Solution state ^{1}H NMR spectra were collected on a Bruker AVANCEIII or 300 MHz spectrometer at 298 K. Deuterated solvents were obtained from Cambridge Isotope Laboratories and their solvent residual signals were used as internal references for chemical shifts. The uncertainty in coupling constants (J) for 1H NMR is ± 0.3 Hz. Analysis of all spectra was conducted in MestRe Nova.

Thermogravimetric Analysis (TGA)
Experiments were performed on a TA Instruments Discovery TGA. Approximately 0.33 mg of sample was loaded onto a platinum pan and heated from room temperature to 700 °C at a ramp rate of 20 °C/min under an air flow of 20 mL/min. TGA collections for Zn-Cyc and Cd-Cyc were performed by Dr Eleanor Kearns.

Raman Spectroscopy

Samples were analysed using a Renishaw Raman InVia Reflex Microscope (Renishaw plc., Wotton-under-Edge, UK), equipped with an air-cooled charge-coupled device (CCD). The spectrometer is fitted with holographic notch filters and two gratings (2400 l/mm (visible) and 1200 l/mm (NIR)). The attached microscope is a Leica DMLM equipped with five objectives (× 100/0.85 NA, × 50/0.75 NA, × 20/0.40 NA, × 10/0.25 NA × 5/0.12 NA) and a trinocular viewer that accommodates a video camera allowing direct viewing of the sample. The spectrometer was controlled by PC using the instrument control software (Renishaw WiRE™, Version 4.4). Before data collection the instrument was calibrated using a silicon internal standard.

Sample excitation was achieved using a XTRA NIR laser (TOPTICA Photonics AG, Graefelfing, Germany) emitting at 785 nm. Spectra were recorded using the 50× objective over the spectral range of 400 to 1700 cm^{-1} with the accumulation of 5 scans, 10 s exposure and a laser power of 0.5 % mW. Spectra were not corrected for instrument response.

Oil Immersion Raman Spectroscopy
Samples were immersed in silicone oil before excitation. Sample excitation was achieved using a XTRA NIR laser (TOPTICA Photonics AG, Graefelfing, Germany) emitting at 785 nm. Spectra were recorded using the 50× Oil objective over the spectral range of 400 to 1700 cm^{-1} with the accumulation of 5 scans, 10 s exposure and a laser power of 0.5% mW. Spectra were not corrected for instrument response.

Powder X-Ray Diffraction (PXRD)
Powder X-Ray diffraction (PXRD) patterns were measured on a STOE STADI P diffractometer operating in Debye-Scherrer geometry with Ge(111) monochromated Mo Kα1 radiation (λ = 0.70930 Å) and three Mythen 1K strip detectors in a stationary mode, covering a 2θ range of 0–55°. Samples comprised of crystals were ground into a powder and contained in flame-sealed thin-walled glass capillaries that were rotated during the measurements.

Variable Temperature PXRD
X-ray powder diffraction (PXRD) patterns were measured on a STOE STADI P diffractometer as previously described. Sample temperature control was achieved using an Oxford Cryosystems nitrogen Cryostream 700 Plus (80–500 K) to deliver a stream of dry nitrogen gas over the outside of the capillary.

Diffraction patterns were collected in 20 K increments with ten minute exposure times between the range 180–440 K. Samples were loaded as bulk polycrystalline powders suspended in Ethanol into 0.5 mm glass capillaries. Centrifugation was applied at 1000 rpm to compact the polycrystalline powders before the capillaries were flame-sealed to prevent solvent loss.

Single Crystal X-Ray Diffraction (SCXRD)
SCXRD data for Zn-Pad and Zn-Cof was collected on the MX1 Beamline Australian Synchrotron diffractometer. Data for Zn-Cyc was collected on a Rigaku Oxford Diffraction Synergy Custom DW system, HyPix6000HE using Cu-K_α1 (1.5406 Å) radiation.

In all collections single crystals were immersed in paratone oil before being mounted on a nylon loop and attached to the goniometer head. The crystal was kept at 100.0(2) K during data collection. Using Olex2,[112] the structure was solved with the SHELXT[113] structure solution program using Intrinsic Phasing and refined with the SHELXL[114] refinement package using Least Squares minimisation. Dr William Lewis provided the structure solution for Zn-Cyc and provided assisted for the solutions of Zn-Pad and Zn-C.

Electrochemistry
Solution and solid state cyclic voltammetry and squarewave voltammetry experiments were performed with a BASi Epsilon Electrochemical Analyser using ferrocene /ferrocenium ion (Fc/Fc^+) as an internal reference. Experiments were conducted in a single cell compartment containing a 0.1 M $TBAPF_6$ /MeCN electrolyte solution under an Ar atmosphere. The cell featured glassy carbon working (1.5 mm diameter), a Pt counter, and Ag *quasi*-reference electrodes. Solid state experiments were conducted by immobilising the powdered sample onto the glassy carbon electrode. Squarewave experiments were run with an amplitude of 25 mV, frequency of 15 Hz and step size of 4 mV.

Solid-State Ultraviolet-Visible-Near-Infrared (UV-Vis-NIR) Spectroscopy
UV-Vis-NIR spectra were obtained on an Agilent CARY5000 spectrometer operated by Varian Win UV software. Samples were loaded in a $BaSO_4$ matrix and diffuse reflectance data were collected at room temperature over the range 5000-45000 cm^{-1} at a scan rate of 6000 cm^{-1}/min with a Harrick Praying Mantis attachment. Spectra are reported as the Kubelka-Munk transform. Collections were performed with the assistance of Dr Eleanor Kearns.

Chapter 3. Investigation of a double photocycloaddition in a TTF-based MOF

3.1 Full Factorial Design of Experiments

The method for synthesising $[Zn_2(TDC)_2(Py_2TTF)_2]$,[111] as outlined in Chapter 2, was optimised. $[Zn_2(TDC)_2(Py_2TTF)_2]$ was synthesised as previously reported, by solvothermal reaction of Py_2TTF, $Zn(NO_3)_2 \cdot 6H_2O$ and H_2TDC in DMF:EtOH at 100 °C. Red elongated hexagon plate shaped crystals and dark red diamond shaped plate crystals were obtained after 48 hours.

Some crystals within the batch demonstrated a colour change in response to white light, turning from red to orange, but others showed no response to light. Raman spectra gathered of these two different structures showed a strong fluorescence for the photoreactive samples (Figure 3.1).

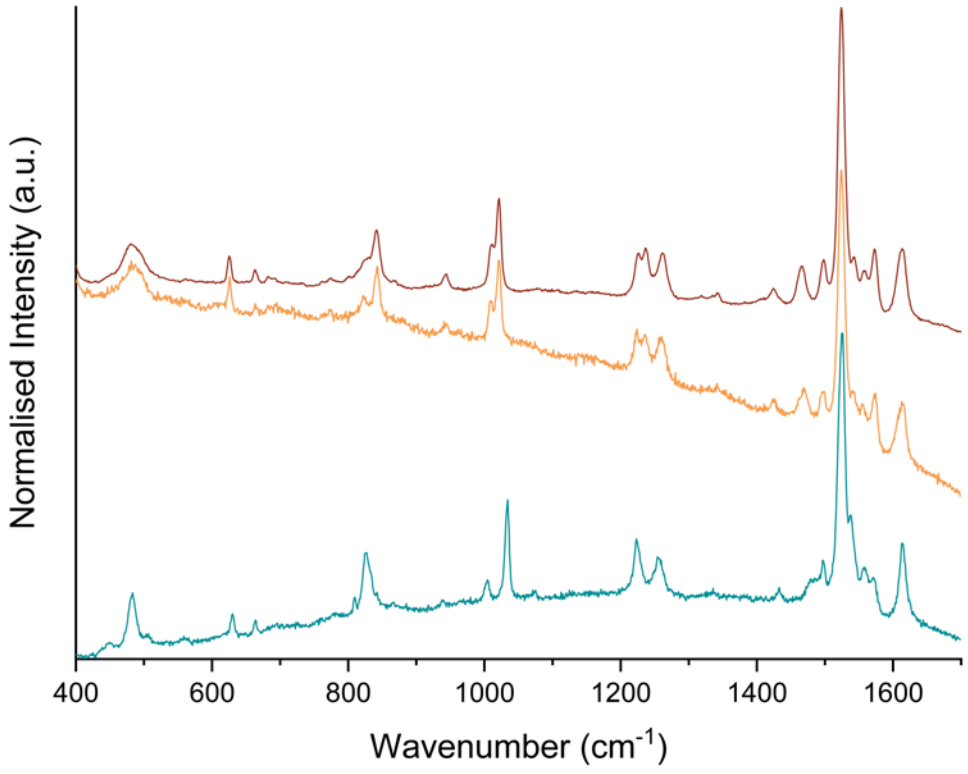

Figure 3.1: Raman spectra of an inert (cyan) and photoresponsive (orange) crystals compared to the previously reported Raman spectrum[111] (magenta)

SCXRD showed two different crystalline materials present $[Zn_2(TDC)_2(Py_2TTF)]$ (Zn-Pad) and

$[Zn_2(TDC)_2(Py_2TTF)_2]$ (Zn-C). Zn-Pad is a paddle-wheel type structure, which does not contain cofacial Py_2TTF pairs, while Zn-C is a pillared structure, which contains cofacial Py_2TTF pairs, and undergoes a structural change in response to light.

3.1.1 $[Zn_2(TDC)_2(Py_2TTF)]$ (Zn-Pad)

$[Zn_2(TDC)_2(Py_2TTF)]$ (Zn-Pad) crystallised in the monoclinic space group $P2_1/c$ with unit cell parameters a = 20.939(4) Å, b = 15.101(3) Å, c = 13.802(3) Å, β = 102.45(3)° and V = 4261.6(16) $Å^3$ (Figure 3.2a). Zn-Pad is comprised of paddlewheel SBUs containing two interconnected eight membered $[-O-C-O-Zn-]_2$ rings, joined throughout the Zn atoms, with TDC units extending out in 4 directions equatorially. Py_2TTF units extend axially, with the TTF units adopting a bent "boat" conformer with the 1,3-dithiole rings at a 24.4° angle to each other forming undulating sheets (Figure 3.2b).

One end of the TTF dimer forms torsion angles with the pyridyl unit ranging between 18.5 - 18.6° and the other forming torsion angles of 0.1 to 11.8°. Pairs of opposing TDC units, through the SBU, are oriented antiparallel to each other. When projected along the a and c-axis, both the TDC units and Py_2TTF units display AA- type ordering, and then projected along the b-axis TDC has AB- type ordering. TDC has an angle of 151° between both dicarboxylates, creating undulating sheets (Figure 3.2c). Zn-Pad is doubly interpenetrated, with the second net lying across the inversion centre (Figure 3.2d).

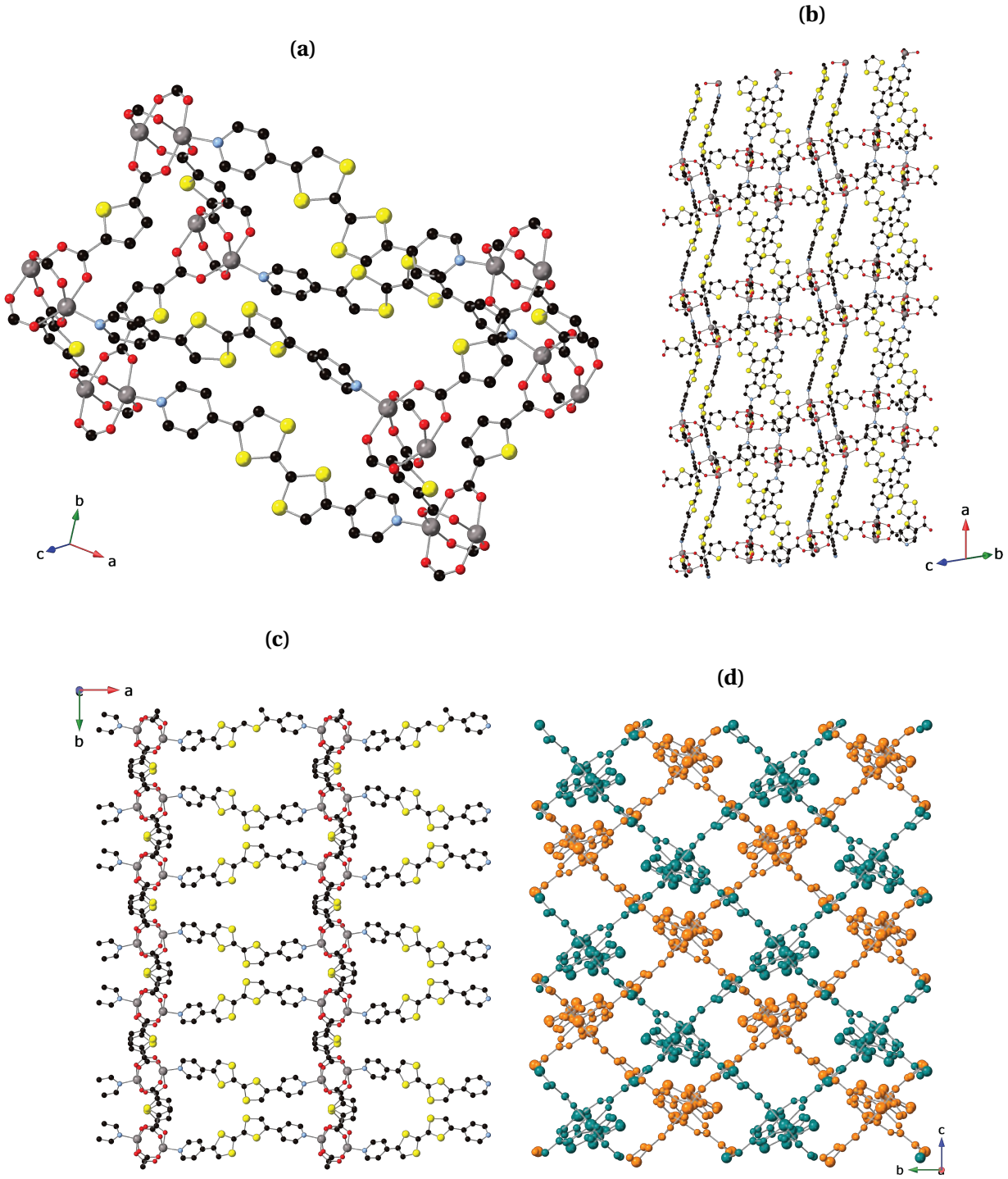

Figure 3.2: (a) A single network of Zn-Pad. (b) Undulating lines of Py_2TTF shown through a 2D slice of the Zn-Pad framework looking through [011]. (c) Undulating lines of TDC in Zn-Pad projected along the *c*-axis. (d) Two-fold interpenetrated network projected along the *a*-axis. Hydrogen atoms are omitted for clarity. Atom colours: C = Black, S = Yellow, N = Light blue, Zn = Grey

3.1.2 Synthesis optimisation for Zn-Pad

Since the reaction conditions formed two different crystal structures, two synthesis optimisation steps were taken, one to selectively obtain Zn-Pad and the other to selectively obtain $[Zn_2(TDC)_2(Py_2TTF)_2]$.

A $2^3 3$ fractional factorial synthetic design was implemented in order to find conditions that would selectively produce Zn-Pad. The variables selected were discrete values and the variations between them considered either low or high. Each variable was denoted by a letter, where samples using the high variant labelled with that letter, such that sample Zn-i was the combination of all low levels, and Zn-abdd was the combination of all high levels.

Two of the factors were chosen to cover the range of reaction conditions used in the synthesis of isostructural frameworks.[38,109–111] Reaction duration (labelled A) was varied between 24 and 48 hours (a), and temperature (labelled D) was either 80 °C, 90 °C (d) or 100 °C (dd). In order to attempt a selective synthesis of Zn-Pad, the stoichiometry was varied to match the stoichiometry (labelled B) seen in the crystal structure of Zn-Pad, between 0.0377 mmol of Py_2TTF and 0.0188 mmol of Py_2TTF (b) compared to 0.0377 mmol of the $Zn(NO_3)_2 \cdot 6H_2O$ and H_2TDC. The factorial design was set up as per Table S.1.

In order to statistically compare the outcomes, numerical evaluation criteria are required. The Scherrer Equation relates the FWHM of an X-ray diffraction peak to the crystallite size (Equation 3.1),[115,116] where D is the crystallite size, K is crystal shape factor, λ is the X-ray wavelength, B is the FWHM of an X-ray diffraction peak in radians and θ is the Bragg angle of that diffraction peak.

$$D = \frac{K\lambda}{B\cos\theta} \tag{3.1}$$

$$D \propto \frac{1}{B} \tag{3.2}$$

The crystallite-shape factor (K) is a value that ranges between 0.62-2.08[117,118] and is based on the crystallite shape and distribution. Since the samples being analysed are multi-phase, both through the presence of Zn-Pad and Zn-C, and through the potential photocyclisation of $[Zn_2(TDC)_2(Py_2TTF)_2]$, a proportional equation (Equation 3.2) is used instead. Optimising for the FWHM of a characteristic peak of the PXRD is correlated to increased crystallite size of the powder sample. The FWHM of the 8.34° peak of the PXRD pattern was used as an optimisation criteria.

Comparing the calculated PXRD patterns for Zn-Pad and $[Zn_2(TDC)_2(Py_2TTF)_2]$, three notable peaks at 3.12°, 5.92° and 8.02° are present in Zn-Pad, but not in $[Zn_2(TDC)_2(Py_2TTF)_2]$, which can be used as an indication of Zn-Pad formation. Samples synthesised at 100 °C showed a peak at 8.02°, and a small peak at 5.92°, indicating some formation of Zn-Pad, though the bulk of the sample remained photoactive (Figure 3.3).

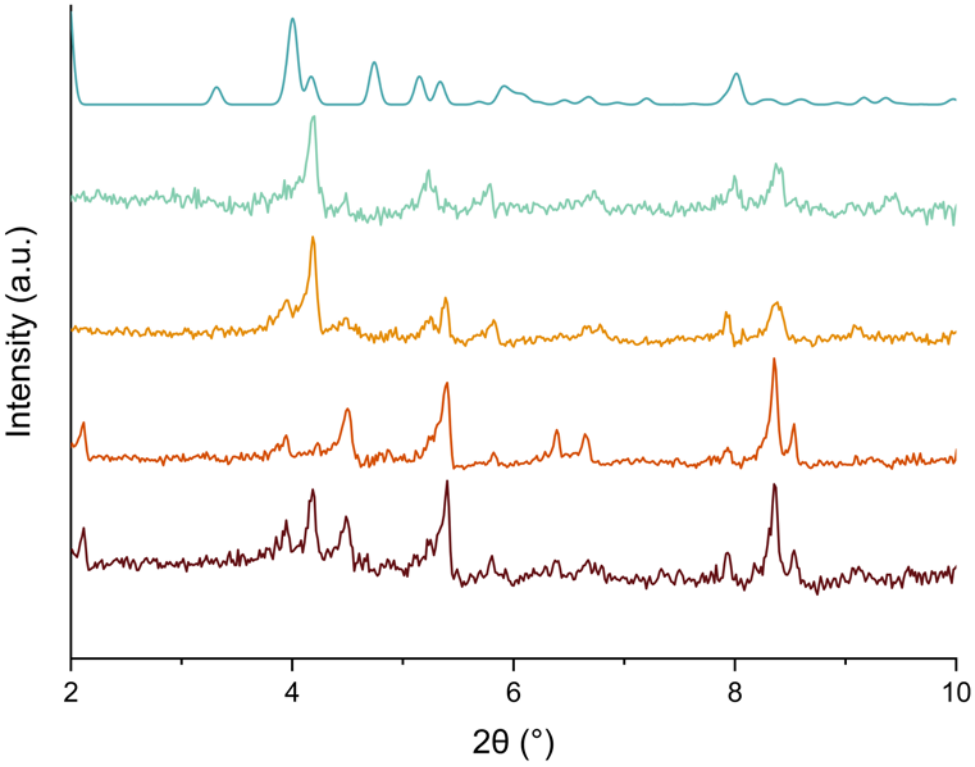

Figure 3.3: PXRD of all samples with a peak at 8.02°. Listed from top to bottom: Calculated PXRD pattern for Zn-Pad, Experimental results for synthesis conditions abdd, bdd, add and dd.

An Analysis of Variance (ANOVA) was performed on the FWHM results of the optimisation, revealing the population means of factors B (stoichiometry) and D (temperature) to be statistically significant (with a p-value = 0.0005 and 0.046 respectively), while factor A (time), along with the secondary and tertiary interactions were not significant.

Table 3.1: Factor means for $2^3 3$ factor optimisation for Zn-Pad

Factor	Level	Mean	Standard Deviation
A (Time, h)	24	0.1079	0.0351
	48	0.1090	0.0431
B (Amount of Py_2TTF, mmol)	0.0188	0.0766	0.0085
	0.0377	0.1403	0.0241
D (Temperature, °C)	80	0.1140	0.0503
	90	0.0937	0.0212
	100	0.1169	0.0416

For factor B, reducing the stoichiometric ratio to 0.0188 mmol of Py_2TTF, while the $[Zn(NO_3)_2 \cdot 6H_2O]$ and $[H_2TDC]$ were kept at 0.0377 mmol had a significant loss of FWHM

broadening, and lower crystallinity than keeping [Py_2TTF] at 0.0377 mmol.

For factor D, synthesis at 90 °C had the best mean result, but lower FWHM, higher peak intensities and higher single crystalinity were seen for samples Zn-i and Zn-a, both synthesised at 80 °C contributing to the high variance of that result.

Zn-Pad could not be selectively obtained for further analysis, *via* this optimisation of synthesis. The highest likely presence of Zn-Pad was shown in reaction conditions ran at 100 °C indicating that Zn-Pad forms as the thermodynamically favourable product.

Bulk phase refinements could not be performed as each synthetic repeat contained at least [$Zn_2(TDC)_2(Py_2TTF)$], [$Zn_2(TDC)_2(Py_2TTF)_2$] and the photoreactive product (Zn-Cyc). Zn-Cyc at that time had not had a crystal structure obtained so no conclusions could be drawn about its calculated PXRD pattern.

3.1.3 Synthesis optimisation for [$Zn_2(TDC)_2(Py_2TTF)_2$]

A $2^3 3$ fractional factorial synthetic design was implemented to find conditions that would selectively synthesise [$Zn_2(TDC)_2(Py_2TTF)_2$] without the formation of Zn-Pad, and reduce crystal cracking, such that crystals suitable for SCXRD would be formed. The factors were chosen to cover the range of reaction conditions used in the synthesis of isostructural frameworks.[38,109–111] Reaction duration was varied between 24 and 48 hours (a), amount of reactants was 0.0377 mmol or 0.0188 mmol (c), and temperature was either 80 °C, 90 °C (d) and 100 °C (dd). The factorial design was set up as per Table S.2.

The FWHM results for this factorial design show no statistical significance (Table 3.2). Despite this, reaction conditions Zn-c showed clear defined improvement compared to other samples. The reaction vessel contained single crystals that were of uniform shape, size and colour, with no residue left on the reaction vessel (Figure 3.4).

Table 3.2: Factor means for $2^3 3$ factor optimisation for [$Zn_2(TDC)_2(Py_2TTF)_2$]

Factor	Level	Mean	Standard Deviation
A (Time, h)	24	0.0774	0.0071
	48	0.0731	0.0157
C (Amount, mmol)	0.0188	0.0739	0.0152
	0.0377	0.0766	0.0085
D (Temperature, °C)	80	0.0782	0.0148
	90	0.0744	0.0062
	100	0.0732	0.0154

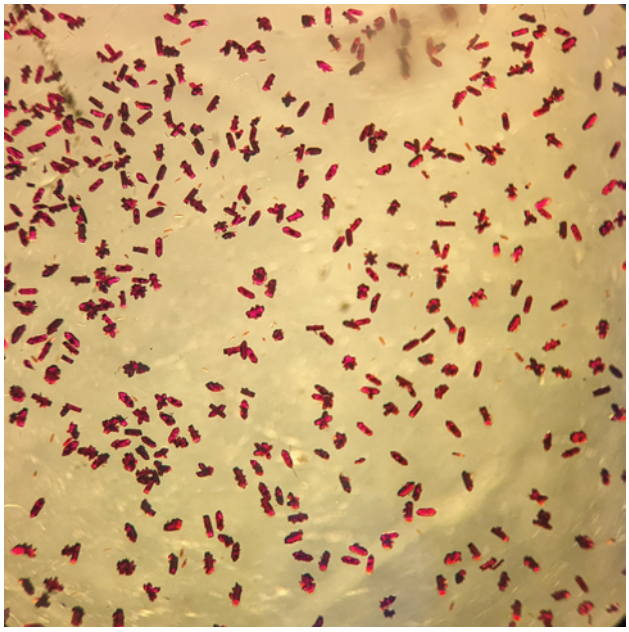

Figure 3.4: Crystals formed within a solvothermal of reaction conditions Zn-c

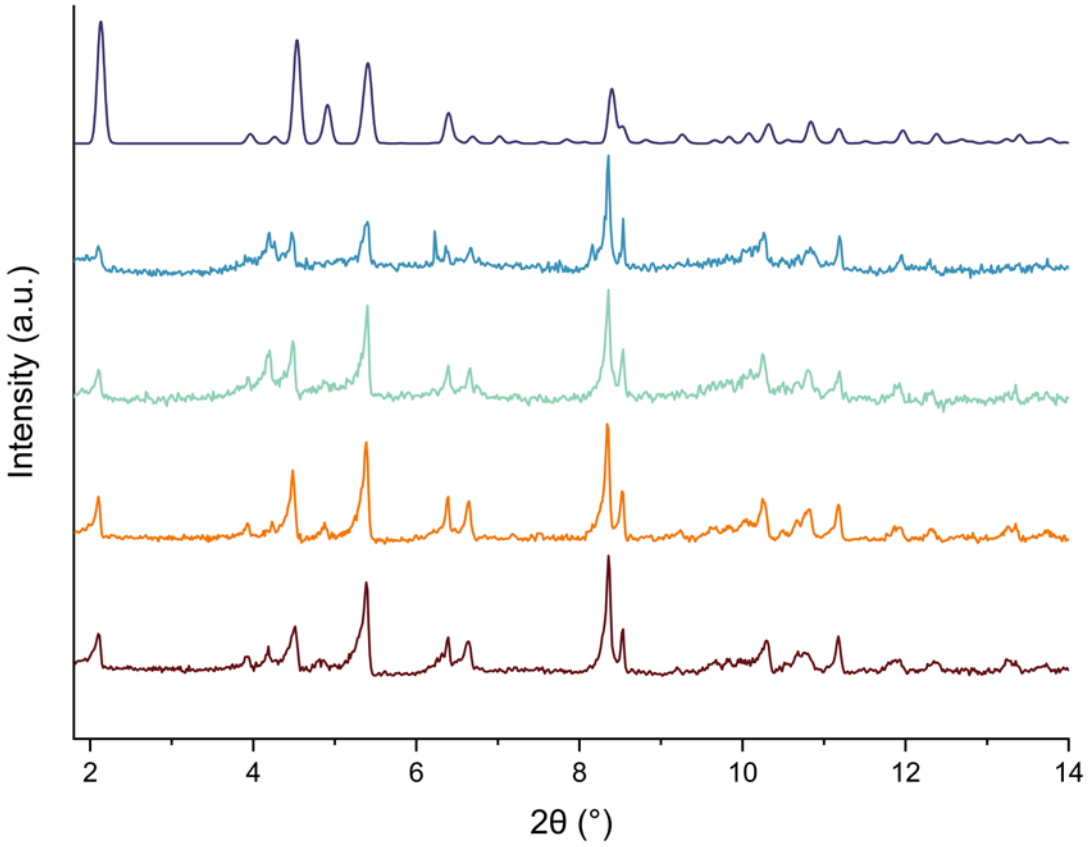

Figure 3.5: Calculated PXRD pattern for $[Zn_2(TDC)_2(Py_2TTF)_2]$ (top, purple) compared to the four experimental results with the lowest FWHM (Synthesis conditions acdd (blue), acd (green), c (orange) and a (bottom, red)).

The FWHM result for Zn-c was 0.06936, which was higher than Zn-a (0.06510), Zn-acd (0.06813) and Zn-acdd (0.05216). Comparison of the PXRD patterns shows that Zn-acd, Zn-a and Zn-c all match peaks present within the calculated pattern, with presence of unexpected peaks at 6.63° and 10.66°, and a different pattern of intensities. These differences are attributed to the presence of the photoreactive product.

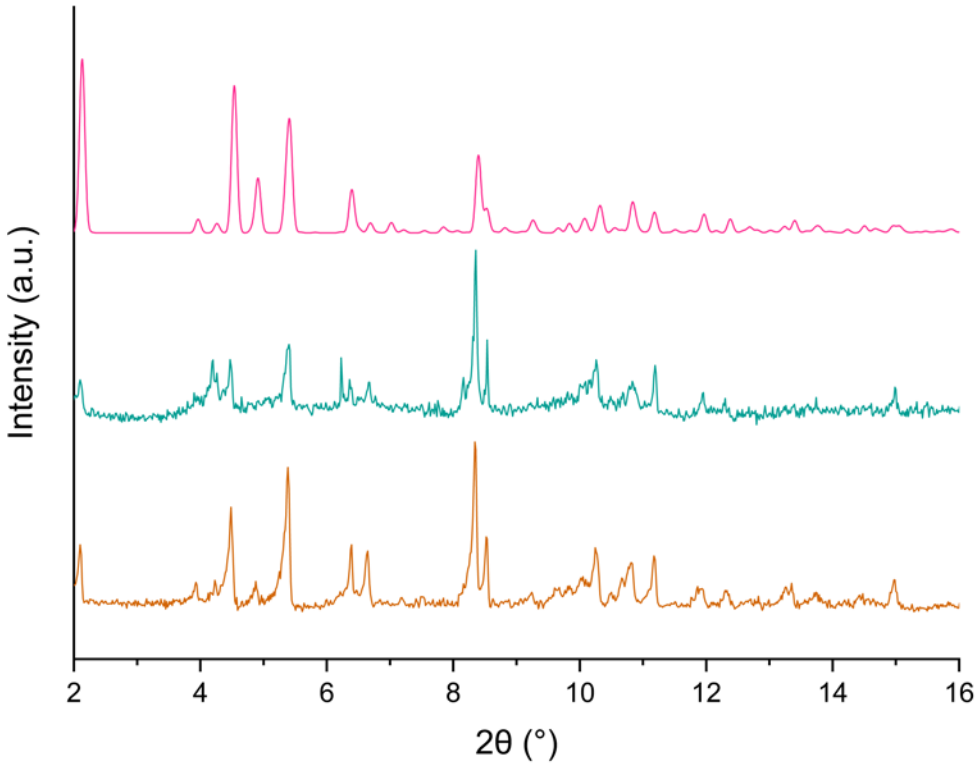

Figure 3.6: The calculated PXRD of $[Zn_2(TDC)_2(Py_2TTF)_2]$ (magenta) compared to PXRD results for the initial reaction conditions (Zn-acdd, cyan), optimised reaction conditions (Zn-c, orange)

Zn-c was selected as the optimal reaction conditions, as it demonstrated uniformity in its product, and well defined PXRD peaks which aligned with the calculated framework PXRD pattern. The initial conditions (Zn-acdd) used had a smaller FWHM of of the 8.34° peak, indicating larger crystallite sizes. The new conditions chosen (Zn-c) have a comparable crystallite size, result in the formation of uniform single crystals, and form a better fit of the calculated PXRD pattern (Figure 3.6). The structure primarily produced by reaction conditions Zn-c is referred to as Zn-C from hereon.

3.2 $[Zn_2(TDC)_2(Py_2TTF)_2]$ (Zn-C)

$[Zn_2(TDC)_2(Py_2TTF)_2]$ (Zn-C) was synthesised by solvothermal reaction of Py_2TTF, $Zn(NO_3)_2 \cdot 6H_2O$ and H_2TDC in DMF:EtOH at 80 °C. Red plate crystals were obtained after 24 hours and structure determined using SCXRD.

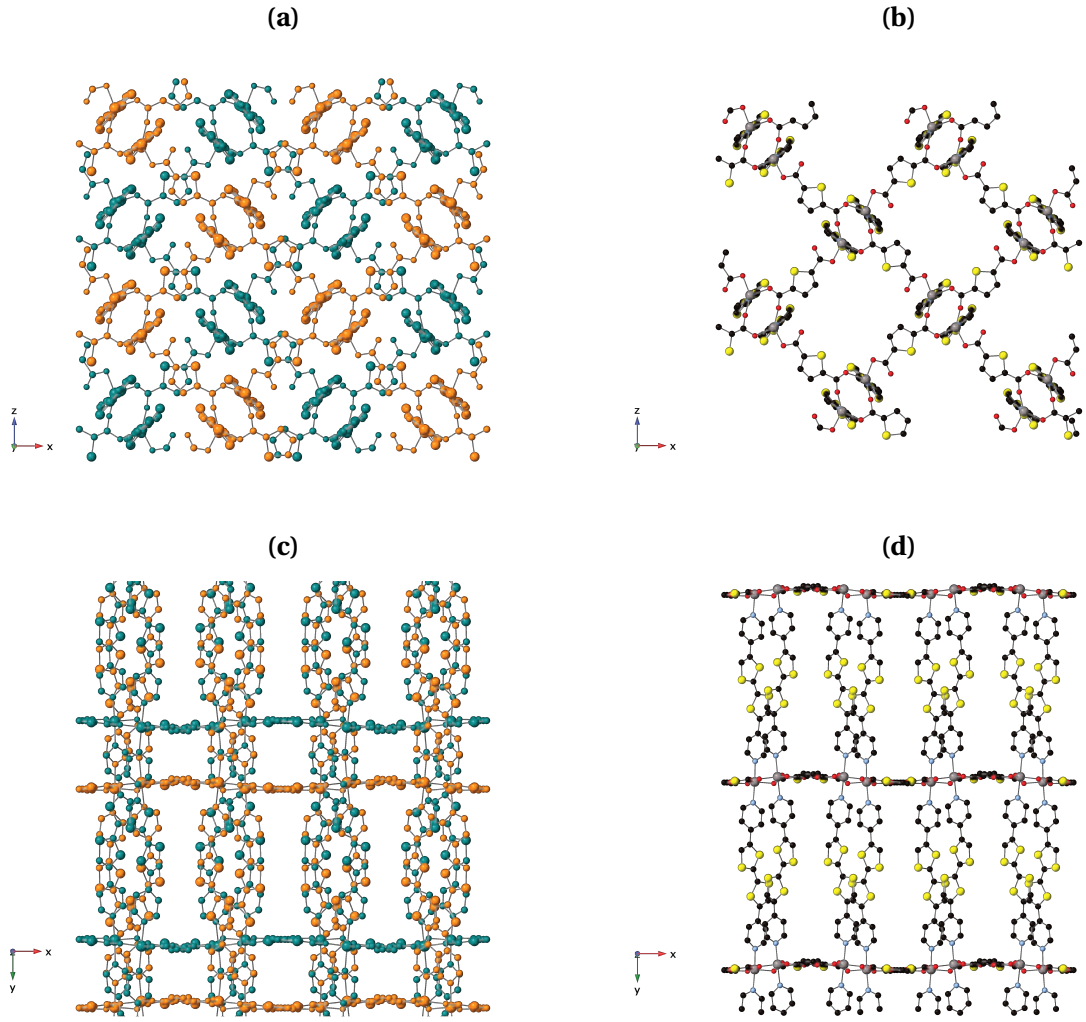

Figure 3.7: (a) Two fold interpenetrated network of Zn-C projected down the *b*-axis.(b) Network of Zn-C projected down the *b*-axis, displaying the rotational ordering of the Py_2TTF and TDC units, only one of the interpenetrated nets is shown. (c) Two fold interpenetrated network of Zn-C projected down the *c*-axis displaying the boat shaped TDC units. (d) Network of Zn-C projected down the *c*-axis, only one of the interpenetrated nets is shown for clarity. Atom colours: C = Black, S = Yellow, N = Light blue, Zn = Grey.

Zn-C crystallised in the orthorhombic space group *Pcc*2 with unit cell parameters $a = 17.763(4)$ Å, $b = 18.906(4)$ Å, $c = 16.404(3)$ Å, V = 5508.9(19) Å^3. Zn-C contains 2D sheets of TDC linked by $[Zn-O-C-O]_2$ clusters. Bridging the 2D planes axially are pairs of cofacial Py_2TTF dimers. Zn-C is doubly interpenetrated (Figure 3.7a), with a second net located halfway along the

unit cell. Pairs of unique TDC units, and pairs of unique $(Py_2TTF)_2$ dimers are oriented in an antiparallel relative configuration (AB) (Figure 3.7d) when projected along the 101 and -101 axes, with the B configuration having a torsion angles of 13.4(2)° and 6.12(16)° with the $[Zn-O-C-O]_2$ clusters, forming a boat shape (Figure 3.7c).

Each pair of Py_2TTF dimers are separated by 3.697(6) Å between the central bond of the TTF units. The individual Py_2TTF units, within the dimer have approximately two fold rotational symmetry along the crystalographic *b*-axis (Figure 3.8a). This lateral displacement causes the reactive C=C pairs within the TTF unit to be separated by 4.12 - 5.57Å. One Py_2TTF dimer had torsion angles of 1.9(2)° and 10.9(2)° between the core TTF and the pyridyl rings, while the other had torsion angles of 11.3(2)° and 18.4(2)°, adopting a far more bent conformation. Zn-C is doubly interpenetrated, forming an enclosed pore space, with window spaces of 1.42 -2.31 Å and was observed to collapse upon desolvation.

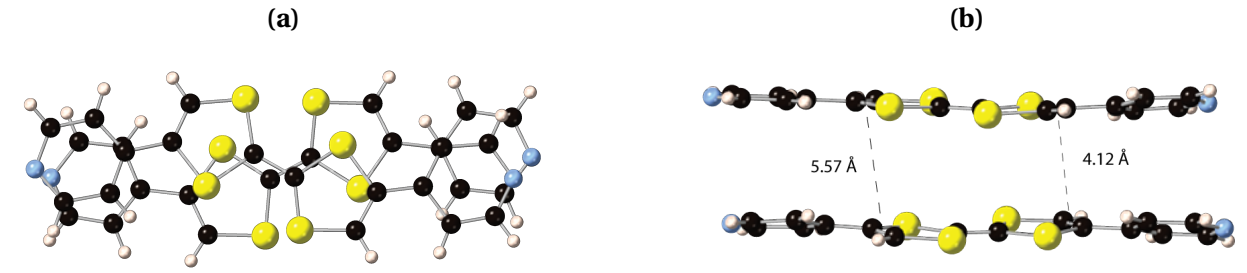

Figure 3.8: (a) Top view of the Py_2TTF dimer; (b) Side view of the Py_2TTF dimer. Atom colours: C = Black, S = Yellow, N = Light blue, Zn = Grey.

The cyclic voltammogram (CV) of Zn-C shows two reversible redox processes at $E_{1/2}$ = +0.56 and $E_{1/2}$ = +0.88. These processes are assigned to the formation of $TTF^{\bullet+}$ and TTF^{2+} respectively.

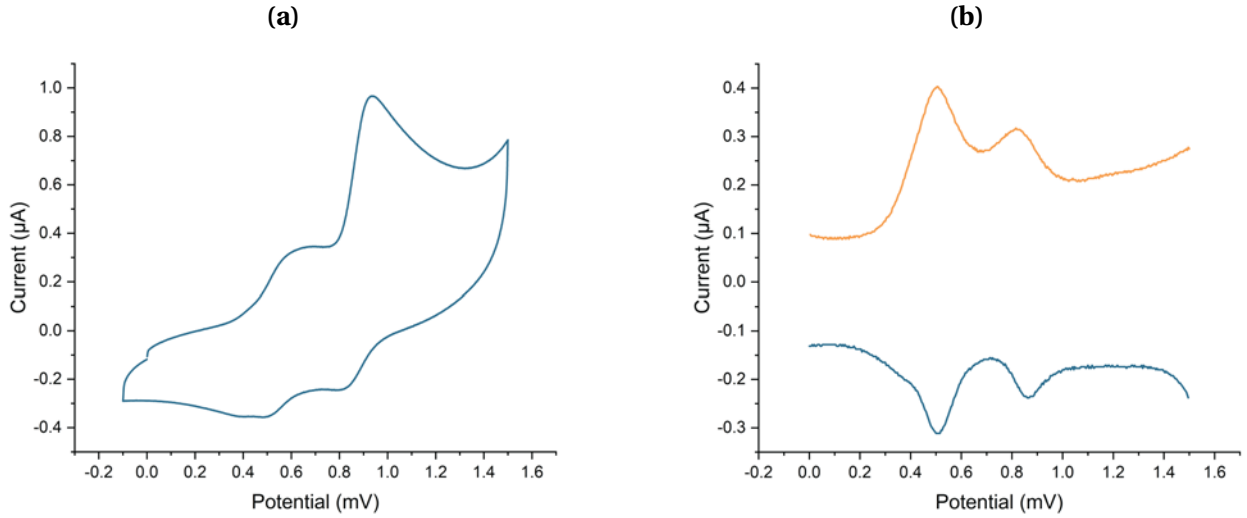

Figure 3.9: (a) CV of Zn-C at 100 mV in 1.0 M $TBAPF_6$ in MeCN. (b) SW of Zn-C in 1.0 M $TBAPF_6$ in MeCN

3.3 $[Zn_2(TDC)_2(Py_4C_{12}S_8H_4)]$ (Zn-Cyc)

When crystals of Zn-C were irradiated with white light, they underwent a colour change from red to yellow, forming crystals of $[Zn_2(TDC)_2(Py_4C_{12}S_8H_4)]$ (Zn-Cyc), suitable for SCXRD.

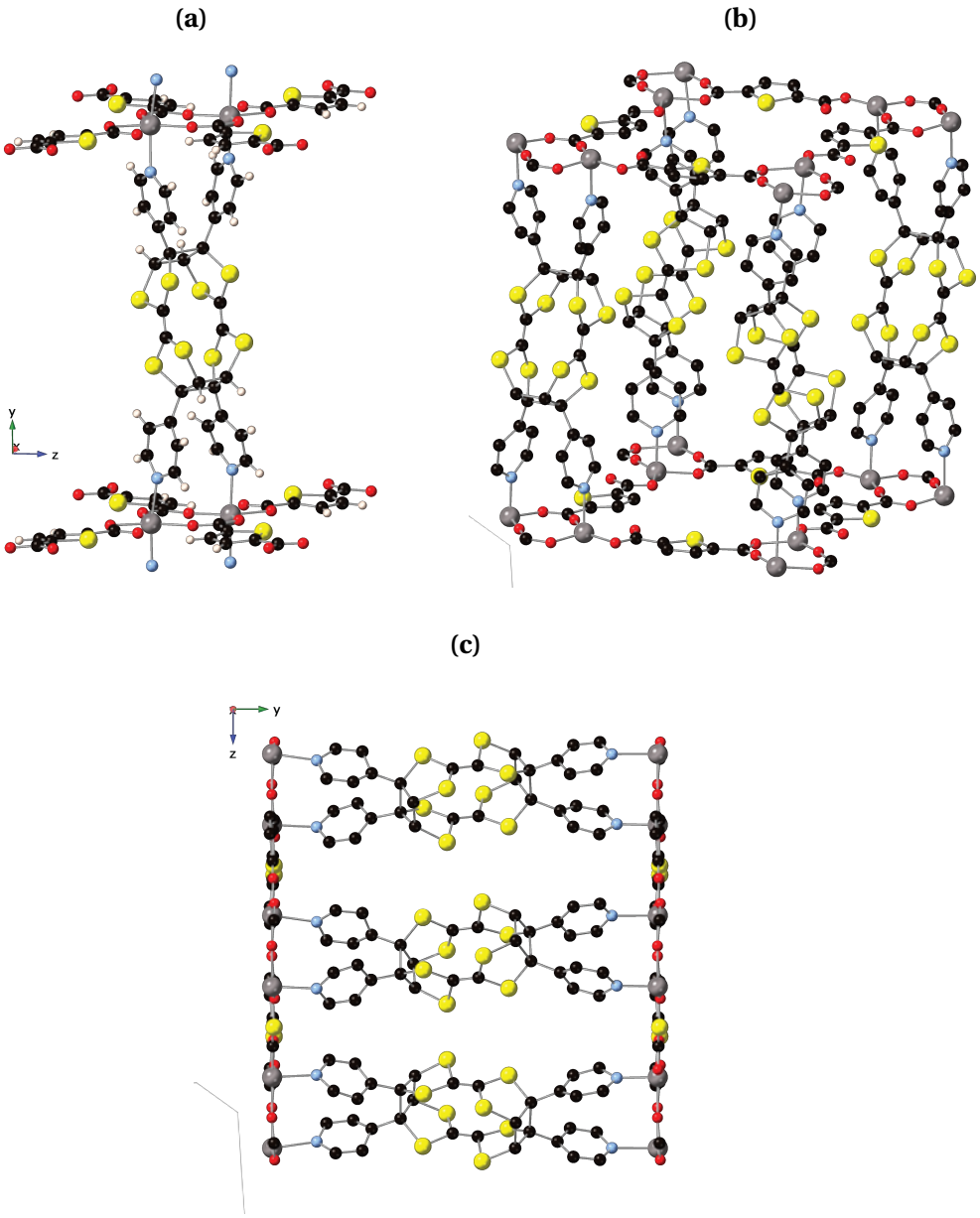

Figure 3.10: (a) A unit of Zn-Cyc. (b) A single framework of Zn-Cyc. (c) Zn-Cyc projected down the *a*-axis. A randomly selected set of disordered $Py_4C_{12}S_8H_4$ ligands is used in each figure. Atom colours: C = Black, S = Yellow, N = Light blue, Zn = Grey.

Zn-Cyc crystallised in the orthorhombic space group *Pcca* with unit cell parameters a = 18.4987(11) Å, b = 18.735(2) Å, c = 15.7143(9) Å. Zn-Cyc is doubly interpenetrated and consists of 2D sheets of TDC linked by $[Zn-O-C-O]_2$ clusters, connected by pillars of

$Py_4C_{12}S_8H_4$. These pillars of $Py_4C_{12}S_8H_4$ are disordered (Figure 3.12) with site occupancy factors of 50%. Comparing to the crossed Py_2TTF ligands in Zn-C, the disordered arrangements of the $Py_4C_{12}S_8H_4$ group indicate that one of the cofacial ligands has crossed to allow photocyclisation.

The TDC units within Zn-Cyc are significantly flatter compared to Zn-C, with torsion angles of 4.95(13)° and 5.03(14)° between the thiophene ring and the $[Zn-O-C-O]_2$ clusters.

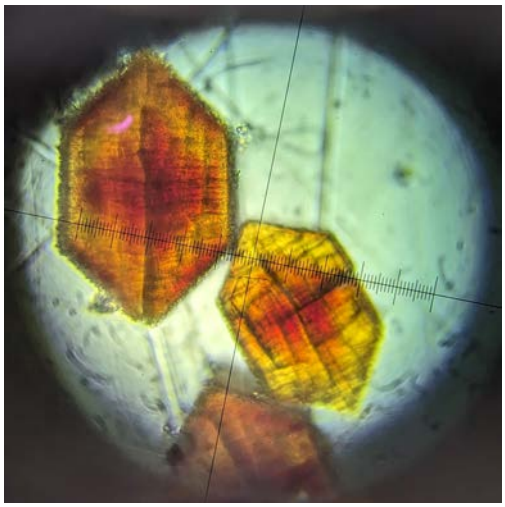

Figure 3.11: Cracks formed in crystals of Zn-Cyc after photocycloaddition.

The structural change from Zn-C to Zn-Cyc resulted in significant crystal cracking (Figure 3.11). The disorder present (Figure 3.12) in the $Py_4C_{12}S_8H_4$ pillars suggests that one of the Py_2TTF units undergoes a flipping or realignment. This structural transition likely contributes to the crystal cracking.

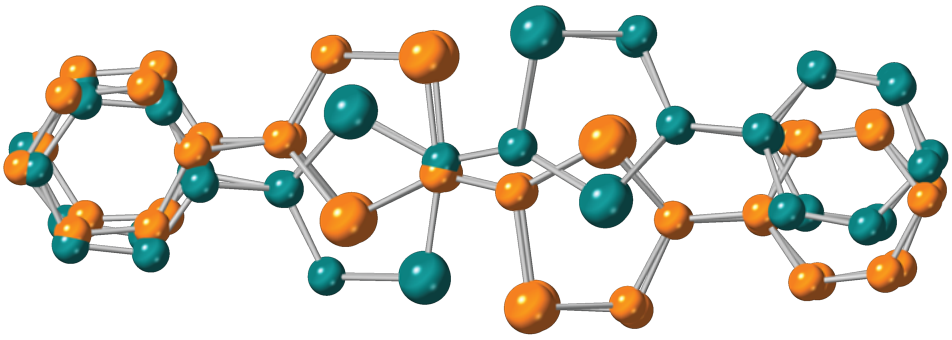

Figure 3.12: Positional disorder of $Py_4C_{12}S_8H_4$ within Zn-Cyc.

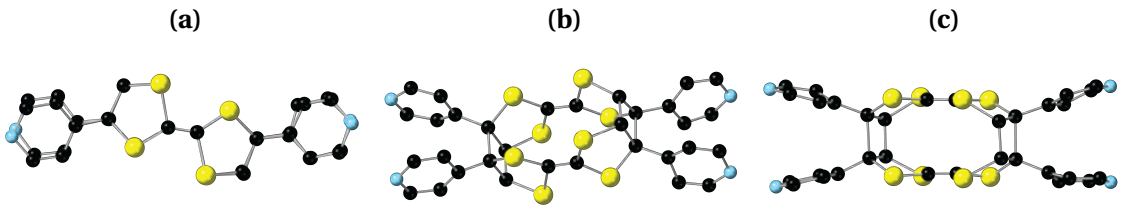

Figure 3.13: The $Py_4C_{12}S_8H_4$ unit as seen from the top (a) looking down the a axis (b) and from the side (c) Atom colours: C = Black, S = Yellow, N = Light blue, Zn = Grey.

3.3.1 Photo-induced cycloaddition of Zn-C to Zn-Cyc

The Py_2TTF dimers are crossed over, leading to no overlap between the olefins required to undergo [2+2] photo-induced cycloaddition (Figure 3.8a). While the distance between the TTF units along the length is 3.697(6) Å, the distance between the photoreactive dimers is 4.12 - 5.57 Å, rotated by 55 - 56° (θ_1), askew by 22.6 - 36.7° (θ_2), and had an offset angle of 56.7 - 76.6° (θ_3). Despite the lack of alignment between these olefins, Zn-C is observed to undergo a double [2+2] photo-induced cycloaddition when exposed to light, to form $[Zn_2(TDC)_2(Py_4C_{12}S_8H_4)]$ (Zn-Cyc).

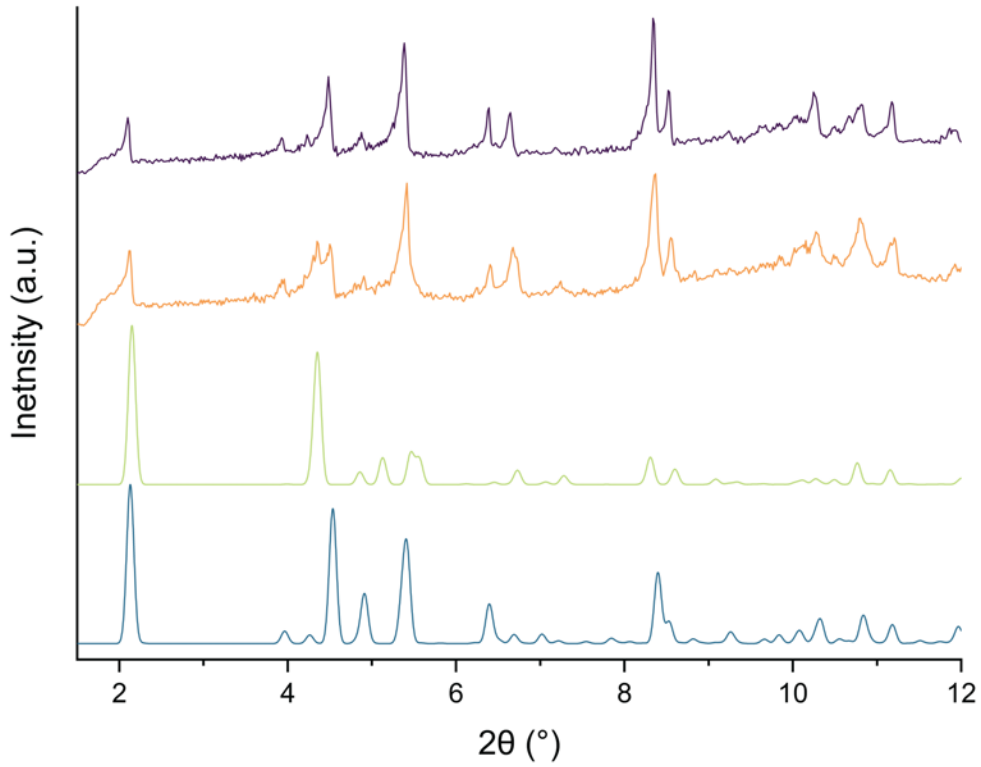

Figure 3.14: Simulated PXRD for $[Zn_2(TDC)_2(Py_2TTF)_2]$ (blue, bottom) and $[Zn_2(TDC)_2(Py_4C_{12}S_8H_4)]$ (green) compared to PXRD of Zn-Cyc (orange) and Zn-C (purple, top)

Zn-C does not undergo full conversion to $[Zn_2(TDC)_2(Py_4C_{12}S_8H_4)]$ as demonstrated by PXRD (Figure 3.14). The presence of peaks at 4.36° and 7.25° indicate formation of Zn-Cyc, however the continued presence of peaks at 3.9°, 4.5° and 6.4° indicate there is still Zn-C present in the sample.

Raman spectroscopy was used so follow the transition from Zn-C to Zn-Cyc, particularly the vibrational modes for Py_2TTF and $Py_4C_{12}S_8H_4$. Comparing the Raman spectra of Zn-C and Zn-Cyc, there is a decrease or disappearance of peaks at 490, 842, 940, 1021, 1230, 1340, 1424, 1498, 1525, 1540, 1570 and 1613 cm^{-1} which match calculated vibrational modes for Py_2TTF within $[Cd_2(bpdc)_2(Py_2TTF)_2]$.[38] Peaks form or grow in intensity at 502, 540, 640, 730, 779, 1078 and 1560 cm^{-1} corresponding to vibrational modes in $Py_4C_{12}S_8H_4$ within $[Cd_2(bpdc)_2(Py_4C_{12}S_8H_4)]$.[38] Unexplained peak changes occur at 558, 804, 818 and 990 cm^{-1}. It is likely that some of these peaks are produced by vibrational modes of TDC, and that the crossed Py_2TTF ligands impact the vibrational modes in Zn-C.

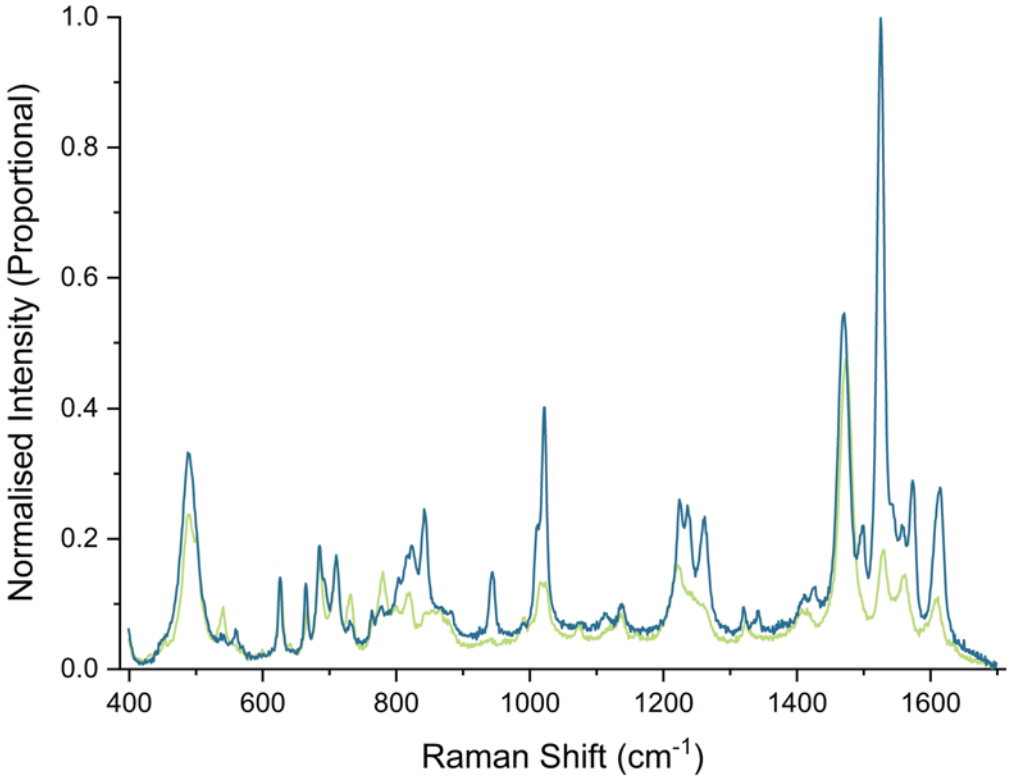

Figure 3.15: Raman spectra of Zn-C (blue) and Zn-Cyc (green) taken from the same crystal under 150 s of 15 W light irradiation.

Spectroscopic analysis of the two materials reveal different UV-vis absorption profiles. This is expected as the two crystals are very different colours. There are three characteristic absorbance bands at 19700 cm^{-1}, 30100 cm^{-1} and 35400 cm^{-1}, which correspond to the reported values[111] (Figure 3.16). The peaks at 19700 and 30100 are assigned to intermolecular transitions of the TTF core. The peak at 35400 cm^{-1} is assigned to $\pi\pi^*$ transitions in TDC and the pyridyl rings. Within Zn-Cyc this peak grows, which could not be assigned.

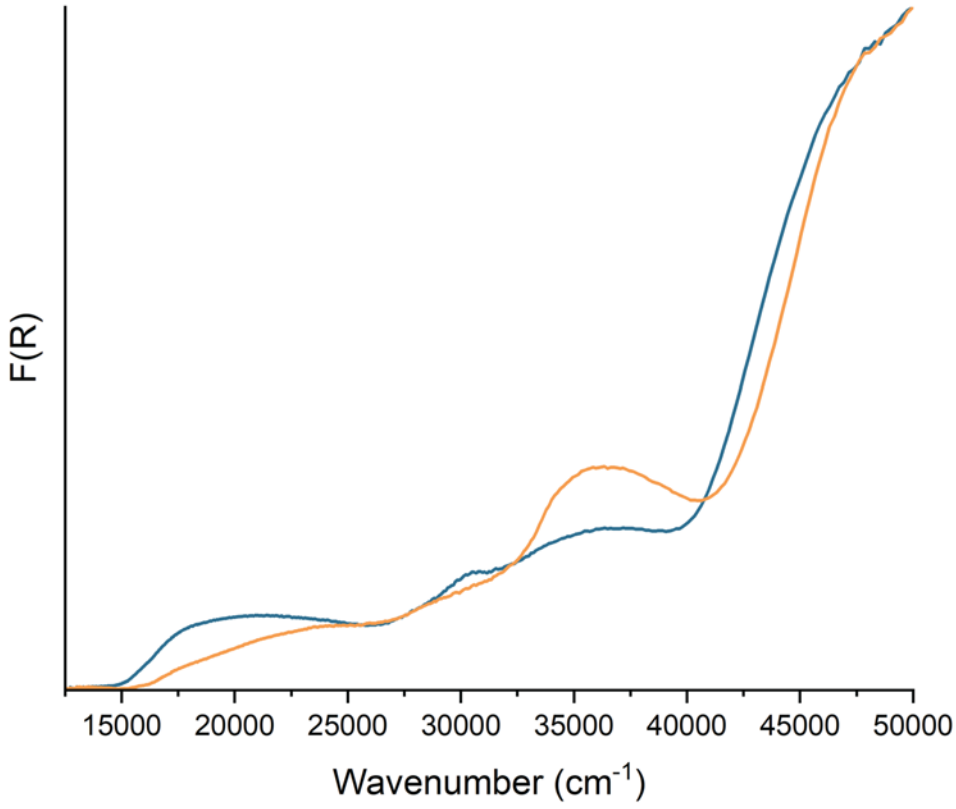

Figure 3.16: Solid state UV-Vis of Zn-C (blue) and Zn-Cyc (orange)

VT PXRD was run on a sample of Zn-Cyc at 20 degree increments until the measurement temperature reached 166.9 °C. Framework collapse occurs between 106.9 °C and 126.9 °C (Figure 3.17) which is where the first solvent loss step begins in the TGA. The solvent loss transition in the TGA peaks at 153 °C. Since the solvents used in the synthesis of Zn-C are Ethanol (b.p. 78 °C) and DMF (b.p. 153 °C), it seems likely DMF is present in pore space and that the framework undergoes collapse upon desolvation. After cyclisation this solvent loss step raises to 206 °C.

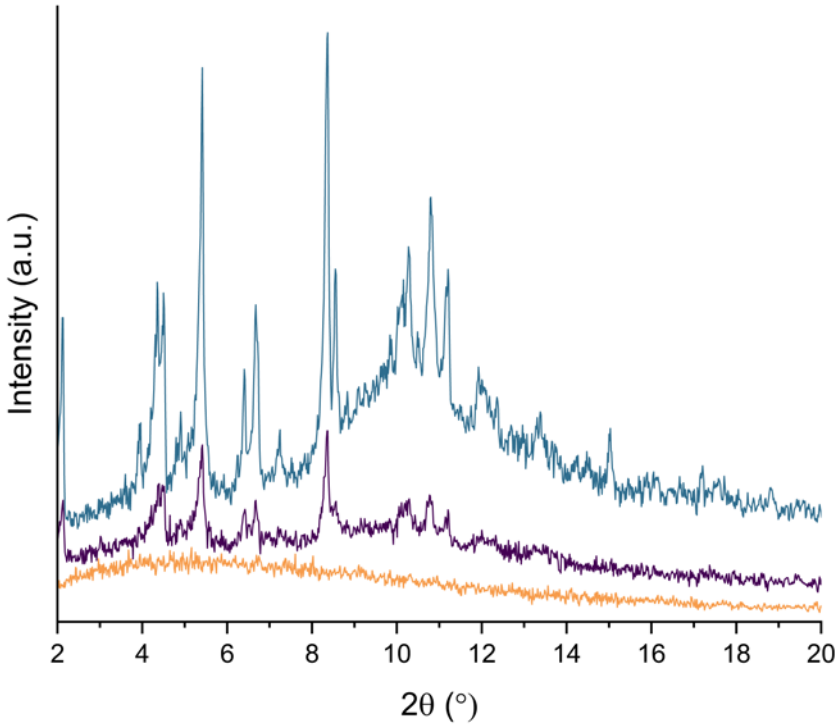

Figure 3.17: Variable Temperature PXRD of $[Zn_2(TDC)_2(Py_2TTF)_2]$ at 6.9 °C (blue), 126.9 °C (purple) and 166.9 °C (orange)

TGA of Zn-C revealed a primary decomposition step at 298 °C, with the cyclised framework showing a small increase in stability, decomposing at 307 °C. Additionally a solvent loss step is seen at 150 °C which is increased to 206 °C in Zn-Cyc. This suggests the structural change from Zn-C to Zn-Cyc increases how difficult it is for solvent to be removed from the pores. Solvent loss of 9.5% indicates 2 molecules of DMF are present per formula unit.

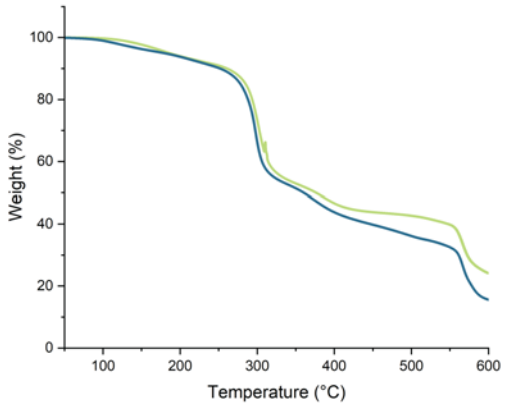

Figure 3.18: TGA of Zn-C (blue) and Zn-Cyc (green)

3.4 Conclusion

Upon discovering the formation of two different crystal structures, within the solvothermal conditions to synthesise Zn-C, two optimisation steps were undertaken. The first optimisation, to synthesise Zn-Pad was unsuccessful. PXRD patterns suggest that reaction conditions that included heating at 100 °C formed some of the paddlewheel structure. This indicates that Zn-Pad is the thermodynamically favourable product. Further optimisations of the synthesis could be performed with different variable ranges in order to selectively form Zn-Pad instead of Zn-C.

Full factorial experimental design could be further improved through multiple replicates of each set of reaction conditions, combined with Mixed-Phase curve fittings on the resulting powder patterns. In further efforts to selectively form Zn-Pad, fractional factorial experimental design can be utilised to analyse a range of impactful variables, while requiring fewer synthetic repeats than a full factorial experimental design.

The second optimising step successfully selectively produced crystals of Zn-C, which were able to undergo a double [2+2] photocycloaddition to form Zn-Cyc. The optimal conditions found were 24 h, 0.0188 mmol of $Zn_2(NO_3)_2 \cdot 6H_2O$, H_2TDC and Py_2TTF and 80 °C. The crystal structure of Zn-Cyc was successfully determined *via* SCXRD. The crossed Py_2TTF dimers in Zn-C rearrange, to form disordered $Py_4C_{12}S_8H_4$ units in Zn-Cyc. The disordered $Py_4C_{12}S_8H_4$ units are symmetry determined, and each have 50% occupancy. This rearrangement would likely bring the Py_2TTF dimers from far outside the geometric Schmidt criteria, to within the geometric Schmidt criteria.

The significant molecular movement of Py_2TTF units within Zn-C to form Zn-Cyc is a clear area for future inquiry. The SCXRD structures presented were collected at 100 K; collecting future crystal structures at higher temperatures, and computational studies can determine the ability of Py_2TTF units to rotate. The crossing of Py_2TTF units within Zn-C is not present in the reported isostructural frameworks $[Cd_2(bpdc)_2(Py_2TTF)_2]$ and $[Cd_2(stil)_2(Py_2TTF)_2]$, so investigations into the impact of the co-ligand angle on the arrangement of the Py_2TTF units are a clear area for future work.

Chapter 4. Kinetics and Cd Analogue

4.1 $[Cd_2(TDC)_2(Py_2TTF)_2]$ (Cd-C)

$[Cd_2(TDC)_2(Py_2TTF)_2]$ (Cd-C) was synthesised by solvothermal reaction of Py_2TTF, $Cd(NO_3)_2 \cdot 4H_2O$ and H_2TDC in DMF:EtOH at 80 °C. Red-yellow plate crystals were obtained after 24 hours. Single crystals suitable for SCXRD could not be obtained. PXRD confirmed that the samples were crystalline. Cd-C was observed to go from red-yellow to yellow-clear when exposed to light. The resulting material is called Cd-Cyc.

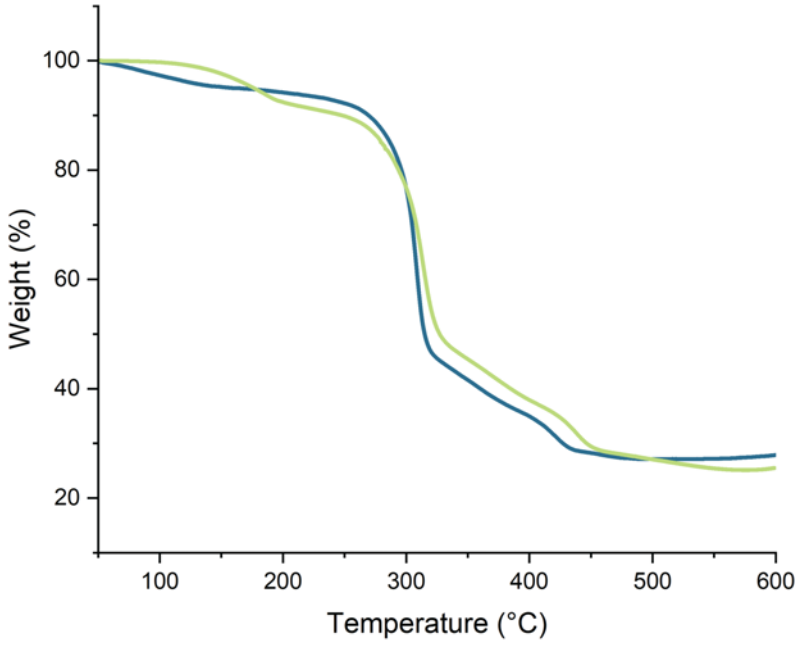

Figure 4.1: TGA of Cd-C (blue) and Cd-Cyc (green)

TGA of Cd-C revealed a primary decomposition step at 308 °C. The transition to Cd-Cyc provided a small increase in stability, decomposing at 314 °C. A solvent loss step at 150 °C for Cd-C and a solvent loss step at 184 °C for Cd-Cyc, indicated that DMF is present within the pores. The solvent loss of 9.6 - 10.6% corresponds to 2 molecules of DMF per formula unit.

The behaviour of Cd-C and Cd-Cyc is similar to Zn-C and Zn-Cyc, with the primary decomposition occurring at 308 °C and 298 °C respectively. This result indicates the the structure contains DMF within its pores, which shift toward higher temperatures after light induced structural transition, supporting Cd-C as an isostructural analogue to the broader series of frameworks.

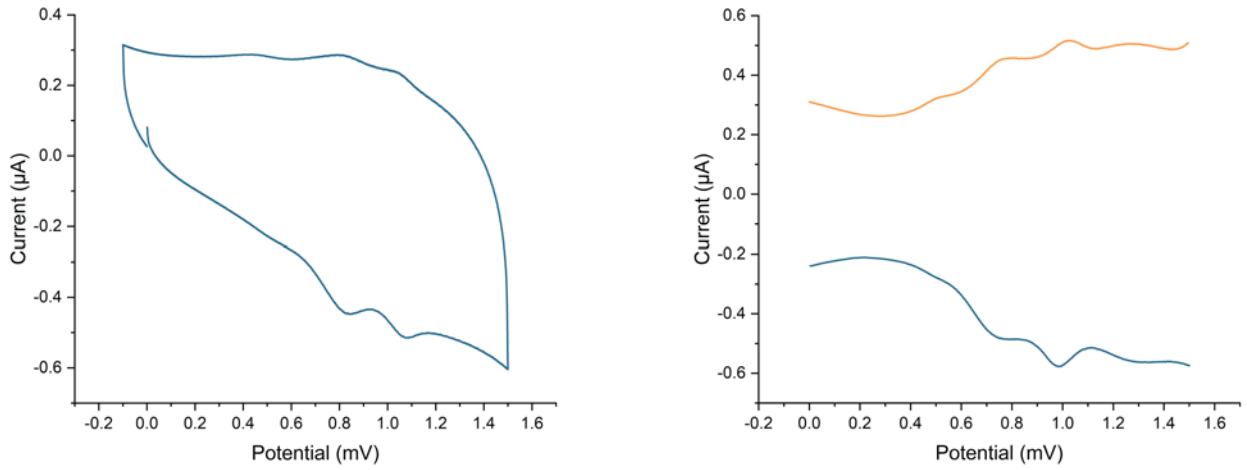

Figure 4.2: (a) CV of Cd-C at 100 mV in 1.0 M $TBAPF_6$ in MeCN. (b) SW of Cd-C in 1.0 M $TBAPF_6$ in MeCN

The CV of Cd-C shows three reversible redox processes at $E_{1/2}$ = +0.47, $E_{1/2}$ = +0.83 V and $E_{1/2}$ = +1.06 V. While the processes at $E_{1/2}$ = +0.83 V and $E_{1/2}$ = +1.06 V are quite pronounced, the process at $E_{1/2}$ = +0.47 V is less so. Due to the low stability of the Cd-C framework, Py_2TTF may be present outside of the Cd-C framework, contributing to the extra redox process.

When Cd-C crystals were irradiated with white light, their colour changed from a red-yellow to a clear-yellow. Cracks in the crystal were observed, unlike the regular and repeatable cracking of Zn-C, Cd-C cracked randomly (Figure 4.3).

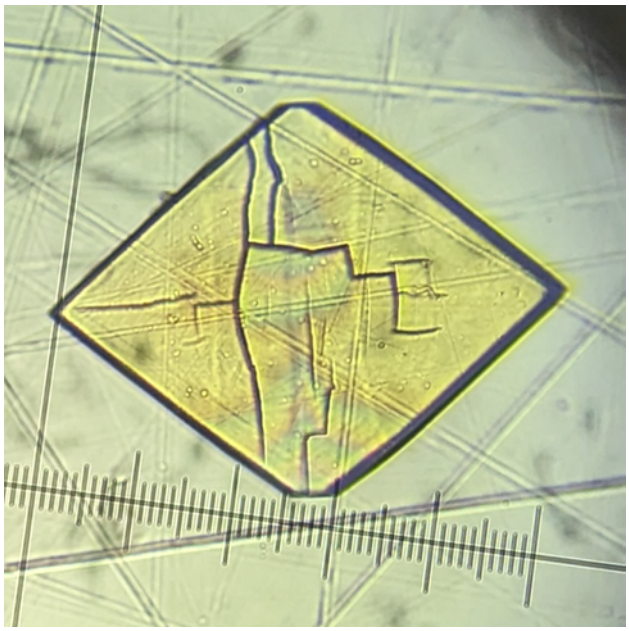

Figure 4.3: Cracking in a crystal of Cd-Cyc

VT PXRD was performed to investigate if the structural change was reversible. Clear peak changes at 6.3°, 8.8°, 11.1°, 11.3° and 11.8° clearly showed a structural change corresponding to the PXRD pattern of Cd-C. Cd-C was reformed by heating to 167 °C, with a loss of crystalinity (Figure 4.4).

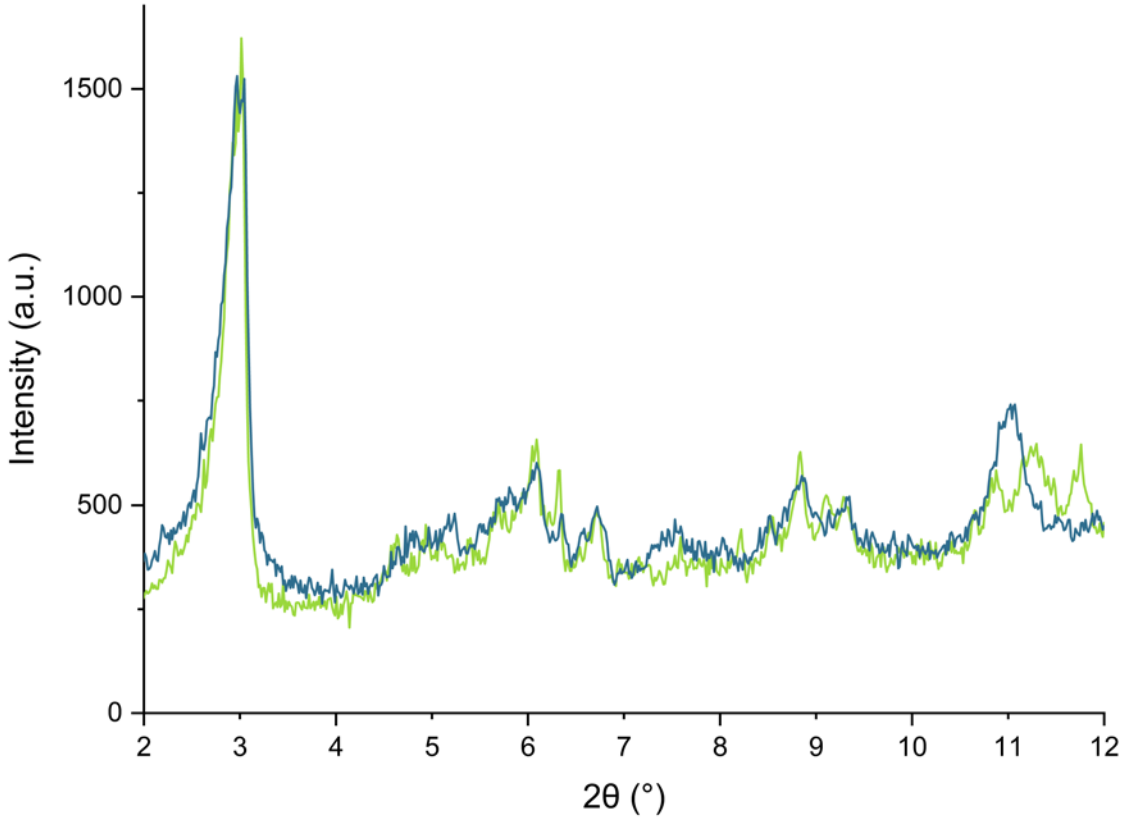

Figure 4.4: Variable Temperature PXRD of Cd-C at 6.9 °C (green) and 166.9 °C (blue)

UV-vis absorption spectroscopy for Cd-C to Cd-Cyc shows a decrease in a 18600 cm^{-1} band, 29900 cm^{-1} shoulder and the 36300 cm^{-1} band, while the Zn-C to Zn-Cyc spectra show a decrease in a 18600 cm^{-1} band, 29900 cm^{-1} shoulder and an increase in the the 36300 cm^{-1} band. The decreasing bands indicate the presence of both Py_2TTF and TDC[119] within the framework, and the diminishing of intermolecular transitions within the TTF core after irradiation, further confirming that the structure of Py_2TTF is altered during the transformation (Figure 4.5a). Comparing the absorbance behaviour of Cd-C and Cd-Cyc to Zn-C and Zn-Cyc reveals very similar absorbance spectra. The differing behaviours of the 36300 cm^{-1} band is attributed to ambient light exposure in the tested sample.

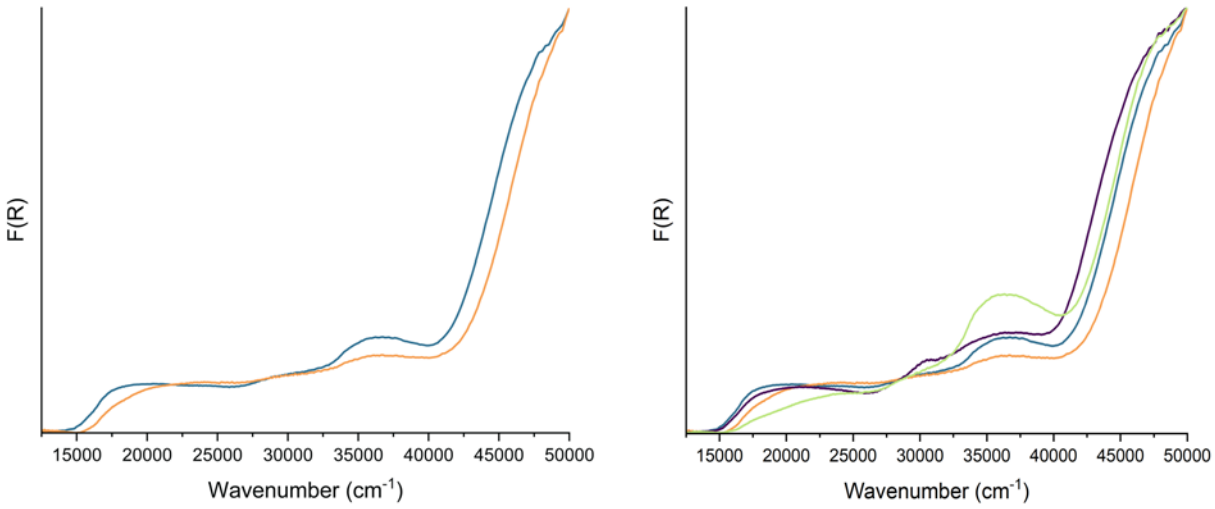

Figure 4.5: (a) Solid state UV-vis of Cd-C (blue) and Cd-Cyc (orange). (b) A comparison of Solid state UV-vis for Zn-C (purple), Zn-Cyc (green) of Cd-C (blue) and Cd-Cyc (orange)

Comparing the Raman spectra of Cd-C and Cd-Cyc, UPDATE COLOUR SCHEME AND SIZING there is a decrease or disappearance of peaks at 487, 939, 1017 1230, 1525, 1570 and 1611 cm^{-1} which match calculated vibrational modes for Py_2TTF within $[Cd_2(bpdc)_2(Py_2TTF)_2]$.[38] Peaks form or grow in intensity at 452, 502, 540, 624, 640, 730, 773, 849 and 1560 cm^{-1} corresponding to vibrational modes in $Py_4C_{12}S_8H_4$ within $[Cd_2(bpdc)_2(Py_4C_{12}S_8H_4)]$.[38] Unexplained peak changes occur at 558, 684, 818, 836, 1254 cm^{-1}. The strong agreement between peak assignments within the isostructural frameworks of $[Cd_2(bpdc)_2(Py_2TTF)_2]$ and Cd-C further support the presence of Py_2TTF pairs that react to form $Py_4C_{12}S_8H_4$ through a double [2+2] photo-induced cycloadditon.

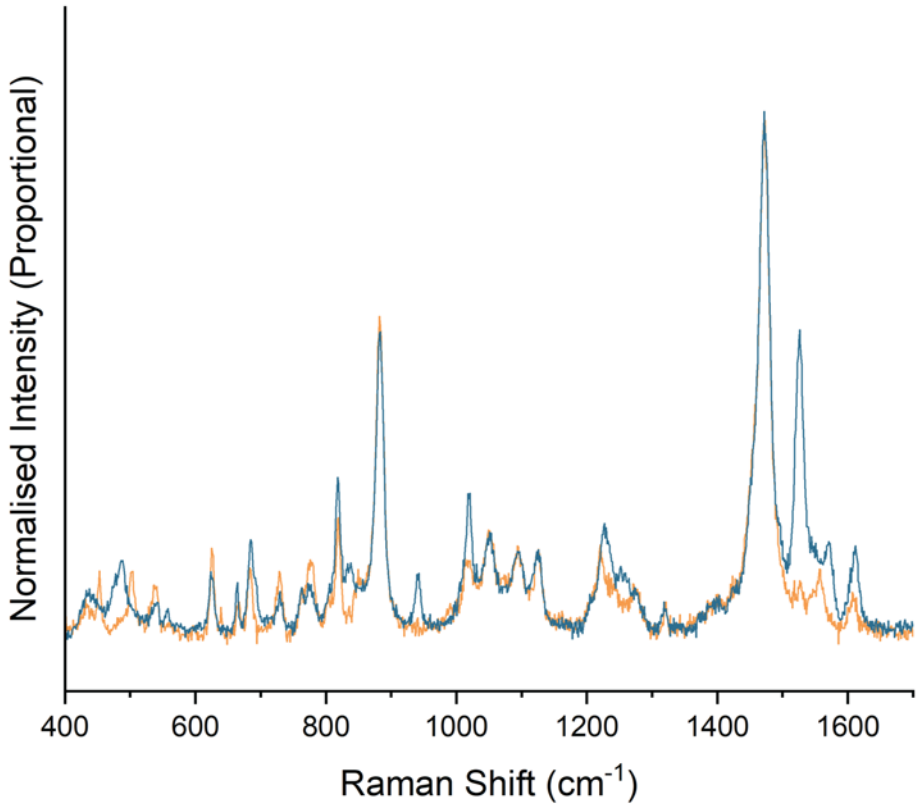

Figure 4.6: Raman of Cd-C (blue) and Cd-Cyc (orange)

A combination of TGA, Raman spectroscopy, solid state UV-vis spectroscopy, CV and PXRD was used to investigate the structures of Cd-C and the product of a light induced transition, Cd-Cyc. These results suggest that Cd-C is another MOF that is able to undergo a [2+2] photo-induced cycloadditon between pairs of Py_2TTF units to form $Py_4C_{12}S_8H_4$. The structural change in Cd-C is reversible, with the reversible change occurring between 146 and 166 °C. Cyclic voltammetry corroborates this with two redox processes at $E_{1/2}$ = +0.83 V and $E_{1/2}$ = +1.06 V.

The current synthesis conditions for Cd-C form crystals as very small thin flat plates, and stress-induced cracking forms during the irradiation of Cd-C, reducing the size of single crystal domains further, making it difficult to perform SCXRD upon the samples. Since Cd-C underwent a very fast photo-induced transition, Cd-C may have high reactivity under X-ray sources which has prevented crystal structure determinations in [2+2] photocycloadditions of TTF-derivatives.[101]

4.2 Kinetics

Kinetic monitoring *via in situ* PXRD

An *in situ* light irradiated PXRD was collected to quantify the kinetics of photocyclisation on Cd-C. Due to the instability of the framework to desolvation the sample was loaded into a 0.5 mm glass capillary. The sample was irradiated with a 470 nm LED over 19 hours, with patterns collected every 20 minutes.

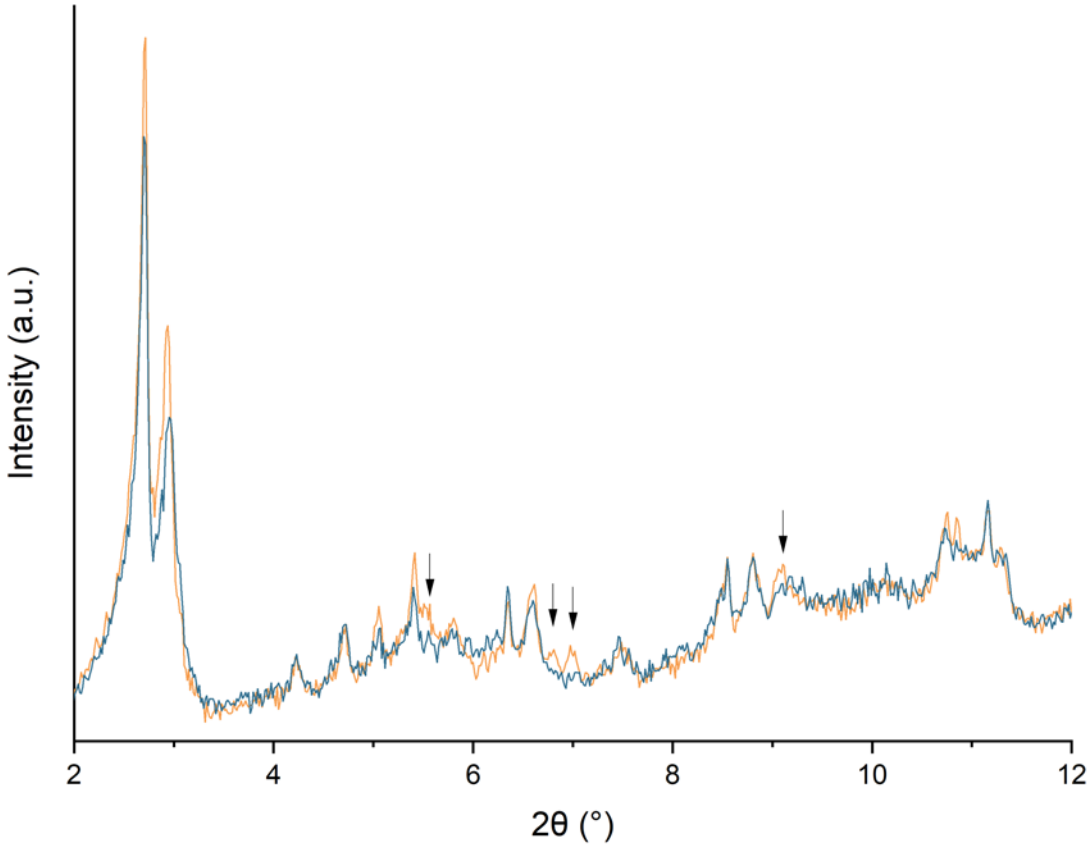

Figure 4.7: PXRD of Cd-C before (orange) and after 19 hours of irradiation (blue) UPDATE DIFFERENTIATE PATTERNS

While the outermost layer of the powder in the capillary showed a colour change, the internal core of the sample was unable to be photocyclised, likely since the external light could not irradiate the centre of the capillary. There was a slight formation of peaks at 5.56°, 6.81°, 6.98° and 9.10° (Figure 4.7).

PXRD could be a powerful technique if it is able to be utilised for kinetics investigations as it provides a direct insight into the structural transformations. In order to enable the external light source to irradiate the entirety of the sample, an extremely small capillary and fine grinding could be used.

Raman Kinetics investigation

Raman spectroscopy was used to investigate the kinetics of the double [2+2] photocycloaddition within Zn-C and Cd-C. Samples were irradiated for 30 s intervals with the built in light of the Renishaw In-Via Raman spectrometer, a Leica LH113 LED with a Pmax of 15 W, at 19% intensity and then Raman spectra were collected.

The focus depth of the microscope determines the local area within which Raman data are collected from. If the microscope had to be refocused due to crystal movement the dataset was abandoned, as it created changes in peak intensity that were not correlated to the photocyclisation. These changes in intensity are due to a differing amount of crystal lattice irradiated to collect the spectra, and a new focus depth may include differing amounts of photocyclisation completeness. Crystals of Zn-C and Cd-C collapsed upon desolvation. To prevent this the crystals were covered in silicone oil, and an oil immersion objective used to remove risk of the desolvation of the crystal throughout the experiment.

Computational work performed on the parent framework $[Cd_2(bpdc)_2(Py_2TTF)_2]$ enables the identification of peaks in the Raman spectra that are useful for determining the rate of photocycloaddition.[38]

According to this work the peak at a Raman shift of 1520 cm^{-1} corresponds the olefin stretching at either end of the TTF core (Figure 4.8),[38] that participate in the double [2+2] photocycloaddition. Since during the photocycloaddition this stretch is lost, a corresponding decrease in the 1520 cm^{-1} peak height is observed.

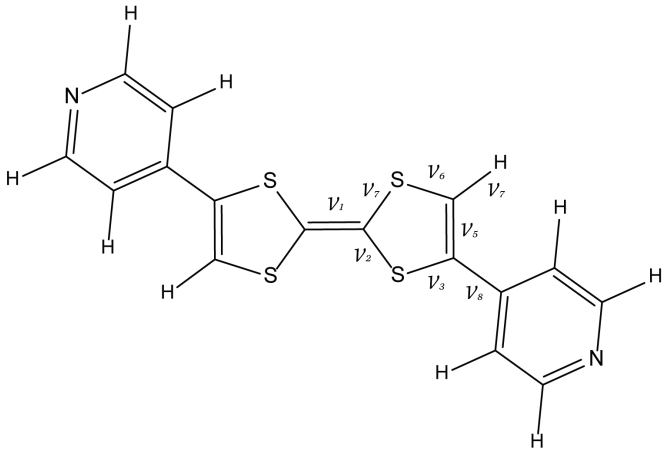

Figure 4.8: Vibrational Modes (ν) of Py_2TTF. Figure reprinted from Nature Communications under a Creative Commons licence.[38]

The peak at a Raman shift of 625 cm^{-1} corresponds to a deformation of the pyridyl rings. This peak remains at approximately the same intensity throughout the duration of the double [2+2] photocycloaddition.[38]

Ambient light exposure was reduced by storing and mounting crystals in an absence of light. Despite this, light was required to locate and focus on each crystal to begin the experiment. Due to this requirement, each crystal used throughout the experiment began with a varying level of Ambient Irradiation sources in the sample preparation, loading and focusing of the

Raman spectrometer.

Differences in crystal size and shape, as well as the focusing depth of the objective all contribute to the intensity of the Raman spectra. In order to compare different repeats, a normalisation step is required, to align the data such that they have the comparable intensities on the basis of the photocyclisation rather than crystal size, shape and focusing depth, and to scale those intensities such that they represent a percentage of conversion.

Multiple analytical repeats, with differing starting values due to ambient light exposure posed an issue for normalisation (Equation 4.1). Here A_i is a measurement from the dataset, A_0 is the minimum measured value and A_n is the maximum measured value.

$$norm(A) = \frac{A_i - A_0}{A_n - A_0} \tag{4.1}$$

Consider a hypothetical photoactive material that undergoes an 100% conversion with ideal kinetics that perfectly follow a JMAK model with n=2, k=1 (Equation 4.2). One sample receives 0 s of ambient light exposure, while the other sample receives 1 s of light exposure before being measured in a kinetics experiment where each sample's conversion percent is collected over 2 seconds.

$$y = 1 - e^{-t^2} \tag{4.2}$$

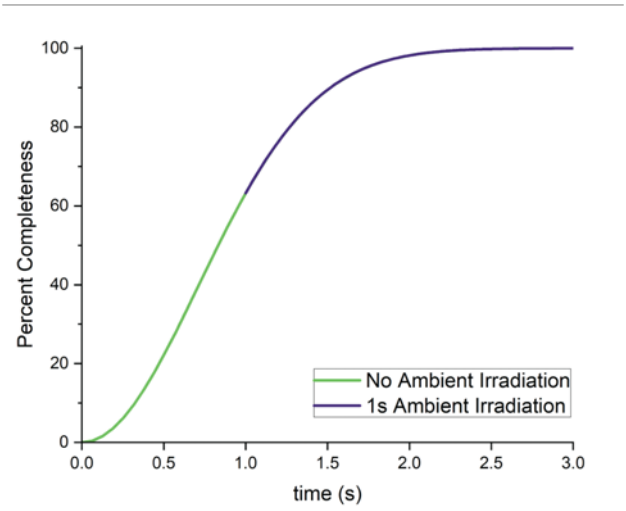

Figure 4.9: Plot of Equation 4.2 over 3 seconds.

The resulting normalisation (Equation 4.1) of both samples (Figure 4.10) results in a vast difference in their final result despite being derived from an identical kinetic process. Applying the JMAK model to the resulting normalised datasets gives an Avrami constant of 1 and a reaction rate of 2.88 for the 1 s sample, while the 0 s sample gives an Avrami constant of 2 and a reaction rate of 1. In this hypothetical case, normalisation *via* Equation 4.1 results in experimental repeats taken with different amounts of ambient light exposure, which model the same process, being misaligned for further analysis.

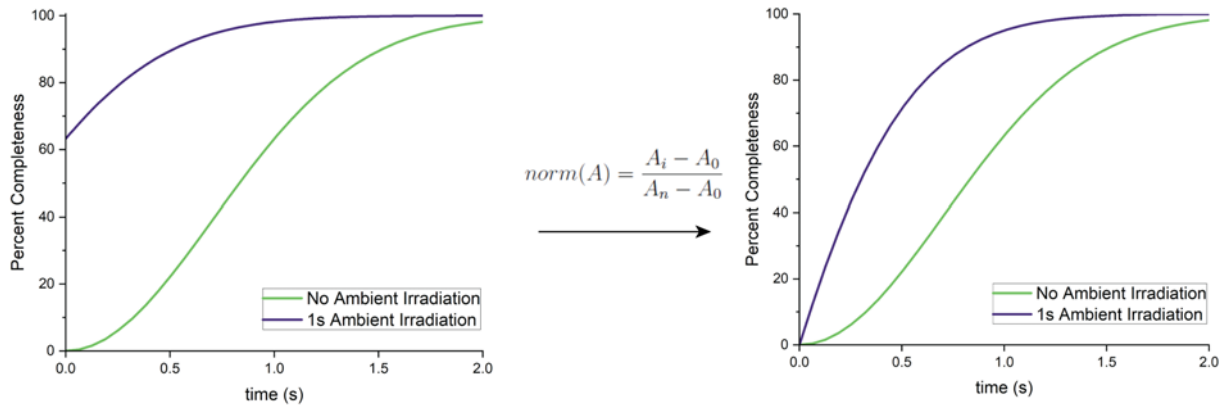

Figure 4.10: Normalisation applied to a sigmoidal kinetic process on differing levels of initial conversion (purple = 1 s of ambient irradiation, green = 0 s of ambient irradiation)

In order to account for this error, alignment of the data such that all datasets share the same intensity can be achieved by taking the integral of the 1520 cm^{-1} peak as a proportion of the integral of the 625 cm^{-1} peak (Figure 4.11). Samples with identical kinetic behaviour with a large amount of ambient light exposure will therefore have smaller initial peak proportions, appearing as translations of the curve along in time. Unfortunately, small differences in ambient light exposure are unable to be differentiated from variance.

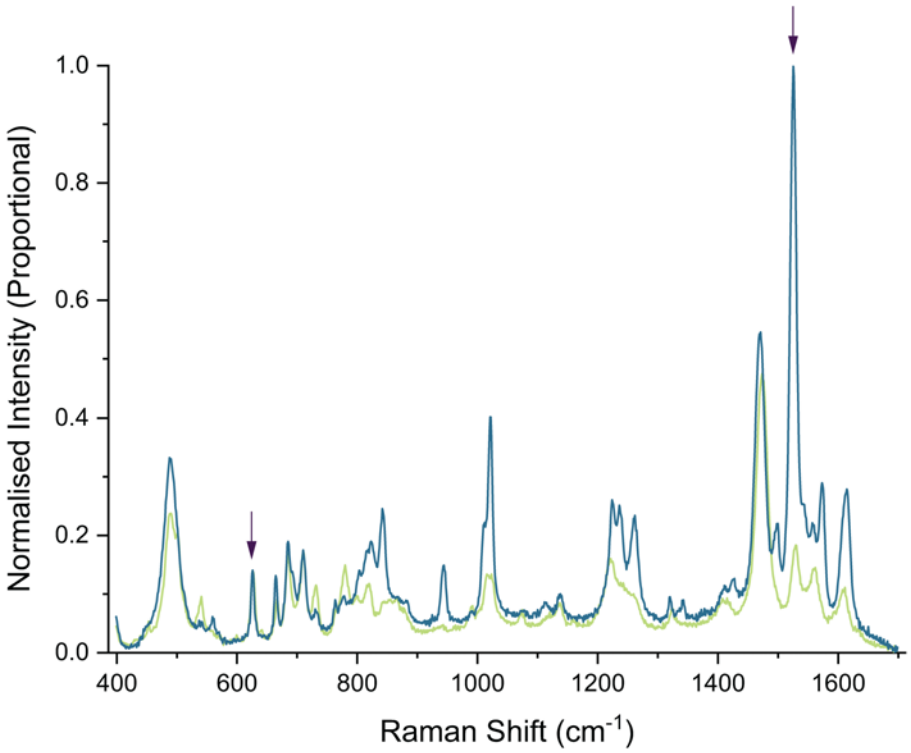

Figure 4.11: Peaks used for Kinetics Analysis shown on Zn-C Raman spectra (blue = 0 s of irradiation, green = 120 s of irradiation)

The proportional scaling of the integral intensities show a strong coherence of the intensities over time, indicating that the difference in ambient irradiation between crystals was minimal.

In some analytical repeats, the 1525 cm^{-1} peak did not reduce to its completed level (Figure 4.11), suggesting an incomplete photocyclisation. These incomplete photocyclisations could be due to framework collapse, through desolvation, or strain and autoihibitive parameters preventing further cycloaddition.[120]

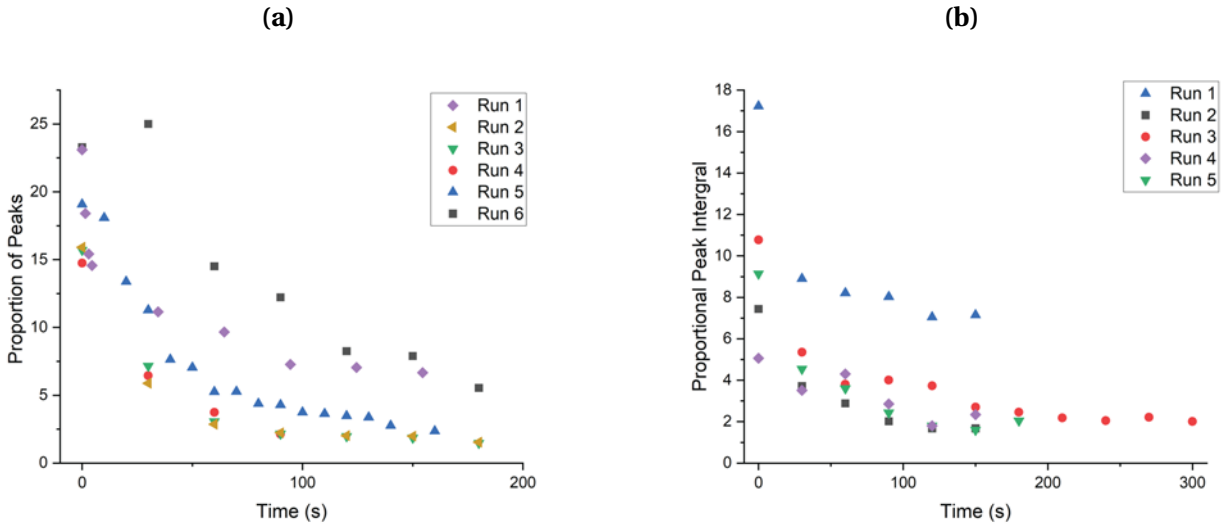

Figure 4.12: The proportional peak intensity of the 1525 cm^{-1} Raman shift to the 625 cm^{-1} Raman shift during light exposure. (a) $[Zn_2(TDC)_2(Py_2TTF)_2]$; (b) $[Cd_2(TDC)_2(Py_2TTF)_2]$

4.2.1 JMAK analysis of Zn-C and Cd-C

The maximum integral peak ratio for Cd-C was 17.22 and the minimum was 1.67. Run 1 only proceeded to 65% completion so was discarded for analysis. All collected datasets for Cd-C were normalised against these values, then linearised for JMAK modelling. The JMAK analysis of Cd-C reveals an Avrami constant of 0.98 ± 0.27 and a Rate constant of 0.38 ± 0.14. An Avrami constant of 1 indicates that the Cd-C photocyclisation is homogeneous and occurs randomly throughout the sample, although with a small degree autoinhibition.

Table 4.1: JMAK results for repeats of Cd-C

Repeat	n	k	R^2
1	1.00	0.21	0.912
2	0.72	0.16	0.969
3	0.82	0.36	0.797
4	1.41	0.56	0.800
5	0.84	0.42	0.481

The maximum integral peak ratio for Zn-C was 25.00 and the minimum 1.55. Run 1 stopped photocyclising at 78% completeness. The collected datasets were normalised against these

values, then linearised for JMAK modelling. JMAK analysis of Zn-C reveals an Avrami constant of 2.03 ± 0.78 indicating the reaction proceeds in a 1-dimensional manner. Due to the large associated error, it is difficult to say whether the reaction proceeds in an autoinhibitive or autocatalyic manner. The measured rate constant was 0.62 ± 0.17 s^{-1}.

Table 4.2: JMAK results for repeats of for Zn-C

Repeat	n	k	R^2
1	1.09	0.30	0.969
2	1.26	0.55	0.950
3	1.92	0.69	0.961
4	2.18	0.76	0.971
5	2.70	0.77	0.981
6	3.08	0.67	0.892

Zn-C appears to form 1-dimensional crystal growth fronts. The Zn-C to Zn-Cyc photocycloaddition shows a large amount of crystal cracking and generates a large unit cell change of 0.74 Å along the *a*-axis and 0.69 Å along the *c*-axis, as well as a likely rearrangement of the Py_2TTF units from antiparallel to parallel. Interestingly the unit cell size change within Zn-C is less than that of both $[Cd_2(bpdc)_2(Py_2TTF)_2]$ and $[Cd_2(stil)_2(Py_2TTF)_2]$. These large unit cell changes have been attributed to strain induced crystal cracking, also present in Zn-C, as well as the autoinhibitive effects seen during photocycloaddition. These changes in the crystal cell likely contribute to the Avrami constant.

Table 4.3: Avrami and Rate constants for Zn-C and Cd-C

Sample	n	n Error	k	k Error
Zn-C	2.03	0.78	0.62	0.17
Cd-C	0.98	0.27	0.38	0.14

Cd-C displays a similar kinetic behaviour as other [2+2] photocyclic frameworks based on $Cd_2(bpdc)_2(Py_2TTF)_2$, with homogeneous crystal growth, and a degree of autoinhibition. The kinetic behaviour of Zn-C is different to the other isostructural photocyclic frameworks, with an Avrami constant indicating 1-dimensional growth, rather than a homogeneous reaction proceeding with autoinhbition. The crossed nature of the Py_2TTF units, and the requirements for those units to rearrange, in order to photocyclise, may play some role in the 1-dimensional propagation of growth.

4.2.2 Finke-Watzky Analysis of Zn-C and Cd-C

Both the JMAK and FW kinetic models use the assumption that the concentration of the product is 0 at time = 0. A Finke-Watzky model that includes a non-zero starting product can be found by taking the condition $[A]_0 + [B]_0 = [A] + [B]$, the rate law 4.3 can be integrated to 4.4.

$$-\frac{d[A]}{dt} = \frac{d[B]}{dt} = k_1[A] + k_2[A][B] \tag{4.3}$$

$$[A]_t = \frac{\frac{k_1}{k_2} + [A]_0 + [B]_0}{1 + (\frac{k_1}{k_2[A]_0} + \frac{[B]_0}{[A]_0}) e^{(k_1 + k_2[A]_0 + k_2[B]_0)t}} \tag{4.4}$$

$$\alpha = 1 - \frac{k_1 + k_2}{k_2 + (\frac{k_1 + k_2}{1 - [B]'_0} - k_2) e^{(k_1 + k_2)t}} \tag{4.5}$$

Then, by taking the condition $[A] + [B] = 1$ the fraction of phase transformation can be found as α (Equation 4.5), where $[B]'_0$ is the percentage of conversion already elapsed during the first measurement. This model is then able to model autocatalytic effects ($k_2 > 0$)[75] and autoinhibitive effects ($k_2 < 0$),[79] as well first order kinetics ($k_2 = 0$). This equation models the behaviour expected for varying values of $[B]'_0$. If $[B]'_0 = 0$, then no prior conversion has happened, and Equation 4.4 equals Equation 1.6, for values $0 < [B]'_0 < 1$ the curve is shifted left, and at $[B]'_0 = 1, \alpha = 1$.

The same datasets used for JMAK analysis, were processed for the FW and autoinhibitive models.

Table 4.4: Rate constants for repeats of Cd-C using an Autoinhibitive model

Repeat	k_1	k_1 Error	k_2	k_2 Error	$[B]'_0$	R^2
1	0.056	0.011	-0.088	0.019	0	0.993
2	0.062	0.036	-0.039	0.043	0.627	0.995
3	0.076	0.013	-0.076	0.015	0.415	0.980
4	0.054	0.026	-0.035	0.032	0.519	0.989
5	0.011	0.128	0	0.147	0.782	0.775

Table 4.5: Rate constants for repeats of Cd-C using an FW model

Repeat	k_1	k_1 Error	k_2	k_2 Error	$[B]'_0$	R^2
1	0.010	0.015	0	0.032	0.134	0.724
2	0.032	0.047	0	0.058	0.630	0.992
3	0.035	0.095	0	0.134	0.427	0.814
4	0.029	0.038	0	0.050	0.524	0.982
5	0	0.136	0.013	0.157	0.783	0.779

Cd-C Repeat 5 was discarded for analysis for both the FW and the Autoinhibitive models, since incomplete conversion cannot be sufficiently modelled. The data was modelled with both an autoinhibitive and FW kinetic model. The autoinhibitive model has a $k_1 = 0.049 \pm 0.027$, $k_2 = -0.050 \pm 0.020$ with an $R^2 = 0.934 \pm 0.053$. The FW model results in $k_1 = 0.026 \pm 0.006$, $k_2 = 0$, $R^2 = 0.878 \pm 0.066$. The resulting R^2 values indicate that the autoinhibitive model provides a better fit for the data. This indicates that the photo induced structural change in Cd-C proceeds with autoinhibition.

The $[B]'_0$ factor for these results models the difference between the highest observed starting peak height, compared to subsequent repeats. Since all samples have some level of ambient light exposure, this value provides a quantification of the variance in the level of light exposure. The average $[B]'_0$ for Cd-C was 0.46 ± 0.26.

Table 4.6: Rate constants for repeats of Zn-C using an Autoinhibitive model

Repeat	k_1	k_1 Error	k_2	k_2 Error	$[B]'_0$	R^2
1	0.010	0.019	0	0.033	0.297	0.082
2	0.064	0.016	-0.035	0.021	0.387	0.999
3	0.038	0.017	-0.009	0.024	0.437	0.999
4	0.033	0.019	0	0.019	0.394	0.998
5	0.025	0.006	-0.003	0.010	0.208	0.978
6	0.008	0.003	-0.001	0.005	0	0.937

Table 4.7: Rate constants for repeats of Zn-C using FW model

Repeat	k_1	k_1 Error	k_2	k_2 Error	$[B]'_0$	R^2
1	0.010	0.019	0	0.033	0.297	0.824
2	0.041	0.022	0	0.032	0.388	0.997
3	0.033	0.019	0	0.027	0.438	0.999
4	0.013	0.010	0.030	0.016	0.396	0.999
5	0.023	0.006	0	0.010	0.213	0.978
6	0.008	0.003	0	0.005	0	0.937

Repeat 1 and 6 were discarded for analysis, since incomplete conversion cannot be sufficiently modelled. Large errors associated with k_1 and k_2 make it difficult to draw conclusions about the reaction rates. The data for Zn-C was modelled using both a FW model ($k_2 > 0$) and an autoinhibitive model ($k_2 < 0$). The autoinhibitive model results in the following values, k_1 = 0.04 ± 0.008, k_2 = -0.012 ± 0.008, with an R^2 of 0.994 ± 0.005. Whereas the FW model result in k_1 = 0.027 ± 0.006, k_2 = 0.007 ± 0.007 with an R^2 of 0.993 ± 0.005. Since the associated R^2 for the curve fits are so similar, it is difficult to draw conclusions about which model to apply, and confirms that the double [2+2] photocycloaddition in Zn-C proceeds without autoinhibitive and autocatalytic effects. The results of both models predict identical behaviour within error beyond 80 s, with a maximum difference of 7.8% conversion.

The $[B]'_0$ factor has an average of 0.28 ± 0.12. Compared to Cd-C, Zn-C was measured with similar levels of photocyclisation across the batch, and few crystals were seen with large levels of ambient light exposure at the batch scale.

Table 4.8: Reaction rate and Autoinhibition reaction rate for Zn-C and Cd-C

Sample	Model	k_1	k_1 Error	k_2	k_2 Error
Zn-C	Autoinhibitive	0.040	0.017	-0.012	0.016
	Finke-Watzky	0.027	0.006	0.007	0.007
Cd-C	Autoinhibitive	0.062	0.010	-0.060	0.026
	Finke-Watzky	0.026	0.005	0	0.017

4.2.3 Comparison of JMAK and FW Autoinhibitive models

Ambient light exposure is difficult to adjust for. In both cases of the FW and JMAK models, the sample space was normalised against the "most" and "least" conversion observed within the sample space, where most and least is evaluated as a proportion of Raman peak heights. This means the resulting values discussed will depict reaction rates faster than the values that would be obtained with a sample with no ambient light exposure. In the case of Cd-C, it has been observed to react over short time frames providing a short window to gather viable data points that represent a low proportion of conversion.

The combination of both a FW and Autoinhibitive model indicated that the photo-induced structural transition in Cd-C proceeded with autoinhibitive effects, whereas the transition for Zn-C had no autoinhibitive effects. This concurs with the result of the JMAK model.

Many steps can be taken to improve the errors associated with these datasets, including a more rigorous crystal selection protocol and more repeats. One spectrum was taken for every 30 s of irradiation. Frequent collections appeared to induce laser degradation of the crystal, so developing experimental methodology for more frequent collections without degradation will vastly reduce the error range.

The use of the 625 cm^{-1} peak to normalise the Raman spectra provides a method to account for crystal shape, size and ambient irradiation with a less rigorous selection protocol. In selecting this peak, careful attention was paid to select a Raman active mode that is unchanged by the photo-induced transition within the framework.

Error fits for FW have far stronger R^2 values compared to the JMAK model, and linearisation reduces the number of data points available, which is vital for extremely fast reactions.

4.3 Conclusions and future work

A novel Cd MOF, Cd-C was obtained through solvothermal synthesis of $Cd(NO_3)_2 \cdot 4H_2O$, H_2TDC and Py_2TTF. The crystal structure of Cd-C could not be obtained. Cd-C was observed to undergo a light induced structural transition, and Cd-C was reformed by heating to 167 °C, confirmed *via* PXRD. Characterisation through Raman spectroscopy, UV-vis spectroscopy and cyclic voltammetry suggest that the transition from Cd-C to Cd-Cyc indicates the loss of Py_2TTF and formation of $Py_4C_{12}S_8H_4$.

The inability to obtain crystal structures for Cd-C and Cd-Cyc make it impossible to determine the structural switch occurring. The small size of the Cd-C crystals and large crystal cracking indicate that an optimisation of the synthesis of Cd-C, to produce larger crystals is one strategy towards obtaining the crystal structures of Cd-C and Cd-Cyc. During SCXRD screenings of Cd-C and Cd-Cyc a rapid loss of diffraction spots was observed, limiting SCXRD collection. Other photocyclic TTF-based crystals have had high reactivity under X-ray sources, preventing the collection of SCXRD data.[101]

Previous JMAK kinetic modelling performed isostructural MOFs $[Cd_2(bpdc)_2(Py_2TTF)_2]$ and $[Cd_2(stil)_2(Py_2TTF)_2]$ obtain values of $n = 0.67 \pm 0.08$, $k = 0.22 \pm 0.08$ and $n = 0.77 \pm 0.11$, $k = 0.19 \pm$

0.04. Cd-C displays similar kinetic properties, n = 0.98 ± 0.27, k = 0.38 ± 0.14, further supporting that Cd-C undergoes a double [2+2] photo-induced cycloaddition. Analysis of Zn-C *via* the JMAK, Finke-Watzky and Autoinhibitive model indicate that Zn-C undergoes 1-dimensional growth with no autoinhibitive or autocatalytic effects. The rearrangement of the crossed nature of the Py_2TTF ligands in Zn-C may contribute to the large difference in kinetics seen between Zn-C and its isostructural frameworks.

The collection of further replicates, with a stricter crystal selection protocol will help to reduce the associated errors across datasets. A modified FW equation and normalisation method was employed to reduce errors introduced through ambient light exposure. Determining wavelengths of light that do not cause [2+2] photocycloaddition in Zn-C and Cd-C would reduce the need for these modified methods, as the assumption that $[B]_0 = 0$ may be remade.

Further work to study the impact of the crossed ligands within Zn-C will provide more insight into the structure function relationship. Further kinetic experiments at variable temperatures and variable pressures may be able to distinguish kinetic factors contributing to the photocyclisation. Determining if Cd-C undergoes a double [2+2] photo-induced cycloaddition enables further comparison of Cd-C and Zn-C. In particular, if Cd-C undergoes a double [2+2] photo-induced cycloaddition, confirming if Cd-C has crossed or cofacial Py_2TTF ligands, enables analysis of the relationship between the metal site and ligand geometries of Py_2TTF. This can be further explored through the development of isostructural frameworks using other metals.

Chapter 5. Conclusions and future work

This work presents a series of investigations into the structural switching within Zn-C. Optimisations of the synthetic conditions were performed to reduce crystal cracking, the product of photocycloaddition, Zn-Cyc was characterised. An attempt to develop a novel framework Cd-C where Cd was incorporated instead of Zn successfully showed evidence of a double [2+2] photo-induced cycloaddition. A study was performed into the kinetics of both systems.

In Chapter **3**, investigations into the synthesis and optimisation of Zn-C were carried out, resulting in characterisation of the structure Zn-Cyc, produced by a double [2+2] photo induced cycloaddition of Zn-C. In order to address challenges with the formation of a second crystal structure, a novel MOF $[Zn_2(TDC)_2(Py_2TTF)]$ (Zn-Pad), a series of optimisations were performed. Two iterations of design of experiments (DoE) used to optimise the synthetic conditions were carried out. One DoE optimised the formation of Zn-C, without Zn-Pad, and another to optimise the formation the Zn-Pad, which was structured in a paddlewheel topology. The optimisation of Zn-Pad revealed that the paddlewheel topology forms as the thermodynamically favoured product. The optimisation of Zn-C successfully produced single crystals suitable for SCXRD. The framework Zn-Cyc, which results from a double [2+2] photo-induced cycloaddition of pairs of Py_2TTF dimers within Zn-C was characterised. Since the pairs of Py_2TTF dimers in Zn-C are crossed, such that the photoreactive olefins are far outside the Schmidt criteria, a significant molecular motion is required, likely through rotation of part or all of the Py_2TTF unit, to form Zn-Cyc. This motion occurs in a disordered fashion, as the resulting structure of the [2+2] photocycloaddition changes the space group of the crystal, from *Pcc*2 in Zn-C to *Pcca* in Zn-Cyc.

Chapter **4** detailed the synthesis and characterisation of the novel MOF $[Cd_2(TDC)_2(Py_2TTF)_2]$ (Cd-C), and the kinetics investigation into the photo-induced structural changes in Zn-C and Cd-C. Cd-C was observed to undergo a light induced structural change. Cyclic voltammetry, UV-vis spectroscopy and Raman spectroscopy confirmed the presence of Py_2TTF within Cd-C, and indicated that $Py_4C_{12}S_8H_4$ was formed upon irradiation with white light. Unlike Zn-C, the structural change in Cd-C was shown to be reversible. These results indicate it is highly likely that Cd-C undergoes a double [2+2] photo-induced cycloaddition, when exposed to white light.

Additionally, Chapter **4** detailed a series of kinetics investigations into the double [2+2] photo-induced cycloaddition within these frameworks. The methodology for Raman spectroscopy based kinetics experiments was expanded upon and a modified version of the FW and Autoinhibitive kinetics models was derived to account for the effects of ambient light exposure.

The kinetic analysis of Zn-C through JMAK gave a reaction rate (k) of 0.62 ± 0.17 and an Avrami constant (n) of 2.03±0.78. Interpretation of the Avrami constant indicates the double [2+2] photo-induced cycloaddition in Zn-C propagates as a 1-dimensional front, and does not indicate any autoinhibitive or autocatalytic behaviour. The FW modelling finds a reaction rate (k_1) of 0.027 ± 0.006 and an autocatalysed reaction rate (k_2) of 0.007 ± 0.007, with the Autoinhibitive model finding a reaction rate (k_1) of 0.040 ± 0.017 and an autoinhibitive reaction rate (k_2) of -0.012 ± 0.016. The very good fits of both models, along with low values of k_2

indicate that there is no autoinhibitive or autocatalytic behaviour, in agreement with the JMAK model.

The kinetic analysis of Cd-C through JMAK gave a reaction rate (k) of 0.38 ± 0.14 and an Avrami constant (n) of 0.98 ± 0.27. Interpretation of the Avrami constant indicates the double [2+2] photo-induced cycloaddition in Cd-C occurs in a random homogeneous manner, and proceeds with autoinhibition. This kinetic process is very similar to the double [2+2] photo-induced cycloadditions in $[Cd_2(bpdc)_2(Py_2TTF)_2]$ and $[Cd_2(stil)_2(Py_2TTF)_2]$. The FW modelling result gave a reaction rate (k_1) of 0.026±0.005 and an autocatalysed reaction rate (k_2) of 0. Autoinhibitive results gave a reaction rate (k_1) of 0.062 ± 0.010 and an autoinhibitive reaction rate (k_2) of -0.060 ± 0.026. Given the poor fit of the FW model, Cd-C is indicated to have an autoinhibitive process occurring within it, in agreement with the JMAK model.

The unusual motion required of Zn-C to photocyclise, as well as the undetermined structure of Cd-C presents several research directions for future work. Developing an isostructural series based on Zn-C may serve to further investigate the structural cause of the crossed Py_2TTF ligands, Cd-C serves as the first step in developing a series using different metal centres, and investigations into the impact of the angle of the co-ligand could be made to further this approach. Computational studies into the energy required for the rearrangement of the Py_2TTF ligands as well as SCXRD studies into the structure of Zn-C at room temperature may elucidate the way in which Zn-C forms Zn-Cyc.

A broad range of wavelengths were used to promote the photocycloaddition in Zn-C, Cd-C and the broader range of isostructural frameworks. Determining a narrower band of wavelengths, or a singularly dependent wavelength which promotes thee [2+2] photo-induced cycloadditions in these systems is a key step in conducting further targeted studies on the conditions needed for structural transitions. Additionally determining visible wavelengths that are incapable of photocyclising these materials enables handling without [2+2] photo-induced cycloadditions occurring due to ambient light exposure.

References

[1] Batten, S. R.; Champness, N. R.; Chen, X.-M.; Garcia-Martinez, J.; Kitagawa, S.; Öhrström, L.; O'Keeffe, M.; Paik Suh, M.; Reedijk, J. *Pure and Applied Chemistry* **2013**, *85*, 1715–1724.

[2] Kondo, M.; Yoshitomi, T.; Matsuzaka, H.; Kitagawa, S.; Seki, K. *Angewandte Chemie (International ed.)* **1997**, *36*, 1725–1727.

[3] Li, H.; Eddaoudi, M.; Groy, T. L.; Yaghi, O. M. *Journal of the American Chemical Society* **1998**, *120*, 8571–8572.

[4] Kalmutzki, M. J.; Hanikel, N.; Yaghi, O. M. *Science Advances* **2018**, *4*, eaat9180.

[5] Hoskins, B. F.; Robson, R. *Journal of the American Chemical Society* **1989**, *111*, 5962–5964.

[6] Kaskel, S. *The Chemistry of Metal-Organic Frameworks*; John Wiley & Sons Incorporated: Weinheim, 2016.

[7] Suh, M. P.; Park, H. J.; Prasad, T. K.; Lim, D.-W. *Chemical reviews* **2012**, *112*, 782–835.

[8] Kim, H. R.; Yoon, T.-U.; Kim, S.-I.; An, J.; Bae, Y.-S.; Lee, C. Y. *RSC Advances* **2017**, *7*, 1266–1270.

[9] Zhao, X.; Wang, Y.; Li, D.; Bu, X.; Feng, P. *Advanced Materials* **2018**, *30*, 1705189.

[10] Hu, Z.; Deibert, B. J.; Li, J. *Chemical Society reviews* **2014**, *43*, 5815–584.

[11] Cui, Y.; Xu, H.; Yue, Y.; Guo, Z.; Yu, J.; Chen, Z.; Gao, J.; Yang, Y.; Qian, G.; Chen, B. *Journal of the American Chemical Society* **2012**, *134*, 3979–3982.

[12] Luz, I.; Llabrés i Xamena, F.; Corma, A. *Journal of Catalysis* **2010**, *276*, 134–140.

[13] Pompe, C. E. L.; Szilágyi, P. A. *Faraday Discussions* **2021**, *231*, 371–383.

[14] He, Z.; Zhao, X.; Pan, X.; Li, Y.; Wang, X.; Xu, H.; Xu, Z. *RSC Advances* **2019**, *9*, 2517–25176.

[15] Li, X.; Liu, J.; Zhou, K.; Ullah, S.; Wang, H.; Zou, J.; Thonhauser, T.; Li, J. *Journal of the American Chemical Society* **2022**, *144*, 21702–21709.

[16] Guillerm, V.; Maspoch, D. *Journal of the American Chemical Society* **2019**, *141*, 16517–16538.

[17] *Chemistry : A European Journal* **2018**, *24*, 16160–16169.

[18] Wang, H.-Y.; Cui, L.; Xie, J.-Z.; Leong, C. F.; D'Alessandro, D. M.; Zuo, J.-L. *Coordination Chemistry Reviews* **2017**, *345*, 342–361.

[19] Montoro, C.; García, E.; Calero, S.; Pérez-Fernández, M. A.; López, A. L.; Barea, E.; Navarro, J. A. R. *Journal of Materials Chemistry* **2012**, *22*, 10155–10158.

[20] Li, H.; Eddaoudi, M.; Groy, T. L.; Yaghi, O. M. *Journal of the American Chemical Society* **1998**, *120*, 8571–8572.

[21] James, S. L. *Chemical Society reviews* **2003**, *32*, 276–288.

[22] Yaghi, O. M.; Li, H.; Eddaoudi, M.; O'Keeffe, M. *Nature (London)* **1999**, *402*, 276–279.

[23] *Science (American Association for the Advancement of Science)* **2002**, *295*, 469–472.

[24] Gianolio, D.; Vitillo, J. G.; Civalleri, B.; Bordiga, S.; Olsbye, U.; Lillerud, K. P.; Valenzano, L.; Lamberti, C. *Journal of Physics: Conference Series* **2013**, *430*, 12134–6.

[25] Cavka, J. H.; Jakobsen, S.; Olsbye, U.; Guillou, N.; Lamberti, C.; Bordiga, S.; Lillerud, K. P. *Journal of the American Chemical Society* **2008**, *130*, 13850–13851.

[26] Lendlein, A.; Trask, R. S. *Multifunctional Materials* **2018**, *1*, 010201.

[27] Bigdeli, F.; Lollar, C. T.; Morsali, A.; Zhou, H. *Angewandte Chemie (International ed.)* **2020**, *59*, 4652–4669.

[28] Janner, A.-M.; van der Sluis, P.; Mercier, V. *Electrochimica Acta* **2001**, *46*, 2173–2178.

[29] Wang, L.; Shima, T.; Hampel, F.; Gladysz, J. A. *Chemical Communications (Cambridge, England)* **2006**, 4075–4077.

[30] Meng, X.; Gui, B.; Yuan, D.; Zeller, M.; Wang, C. *Science advances* **2016**, *2*, e1600480–e1600480.

[31] Ohkoshi, S.-I.; Imoto, K.; Tsunobuchi, Y.; Takano, S.; Tokoro, H. *Nature Chemistry* **2011**, *3*, 564–569.

[32] Modrow, A.; Zargarani, D.; Herges, R.; Stock, N. *Dalton Transactions : an International Journal of Inorganic Chemistry* **2011**, *40*, 4217–4222.

[33] Shimakawa, K.; Inagaki, Y.; Arizumi, T. *Japanese Journal of Applied Physics* **1973**, *12*, 1043–1046.

[34] Burtch, N. C.; Baxter, S. J.; Heinen, J.; Bird, A.; Schneemann, A.; Dubbeldam, D.; Wilkinson, A. P. *Advanced Functional Materials* **2019**, *29*.

[35] Freund, P.; Senkovska, I.; Kaskel, S. *ACS Applied Materials & Interfaces* **2017**, *9*, 43782–43789.

[36] Kim, Y. H.; Ahn, W. J.; Choi, H. J.; Seo, Y. *Colloid and Polymer Science* **2016**, *294*, 329–337.

[37] Zhang, L.; Zhou, Y.; Han, S. *Angewandte Chemie (International ed.)* **2021**, *60*, 15192–15212.

[38] Sherman, D. A.; Murase, R.; Duyker, S. G.; Gu, Q.; Lewis, W.; Lu, T.; Liu, Y.; D'Alessandro, D. M. *Nature Communications* **2020**, *11*, 2808–2808.

[39] Gui, B.; Meng, X.; Chen, Y.; Tian, J.; Liu, G.; Shen, C.; Zeller, M.; Yuan, D.; Wang, C. *Chemistry of Materials* **2015**, *27*, 6426–6431.

[40] Carrington, E. J.; Dodsworth, S. F.; Meurs, S.; Warren, M. R.; Brammer, L. *Angewandte Chemie (International ed.)* **2021**, *60*, 17920–17924.

[41] Brown, J. W.; Henderson, B. L.; Kiesz, M. D.; Whalley, A. C.; Morris, W.; Grunder, S.; Deng, H.; Furukawa, H.; Zink, J. I.; Stoddart, J.; Yaghi, O. M. *Chemical science (Cambridge)* **2013**, *4*, 2858–2864.

[42] Park, J.; Yuan, D.; Pham, K. T.; Li, J.-R.; Yakovenko, A.; Zhou, H.-C. *Journal of the American Chemical Society* **2012**, *134*, 99–102.

[43] Zappe, L.; Schönfeld, S.; Hörner, G.; Zenere, K. A.; Leong, C. F.; Kepert, C. J.; D'Alessandro, D. M.; Weber, B.; Neville, S. M. *Chemical Communications (Cambridge, England)* **2020**, *56*, 1469–1472.

[44] Li, H.-Y.; Xu, H.; Zang, S.-Q.; Mak, T. C. W. *Chemical Communications (Cambridge, England)* **2016**, *52*, 525–528.

[45] Bon, V.; Kavoosi, N.; Senkovska, I.; Müller, P.; Schaber, J.; Wallacher, D.; Többens, D. M.; Mueller, U.; Kaskel, S. *Dalton Transactions : an International Journal of Inorganic Chemistry* **2016**, *45*, 4407–4415.

[46] Roztocki, K.; Bon, V.; Senkovska, I.; Matoga, D.; Kaskel, S. *Chemistry : A European Journal* **2022**, *28*, e202202255–n/a.

[47] Vittal, J. J. *Journal of Photochemistry and Photobiology. C, Photochemistry Reviews* **2023**, *57*, 100636.

[48] Medishetty, R.; Koh, L. L.; Kole, G. K.; Vittal, J. J. *Angewandte Chemie (International ed.)* **2011**, *50*, 10949–10952.

[49] Poplata, S.; Troster, A.; Zou, Y.-Q.; Bach, T. *Chemical reviews* **2016**, *116*, 9748–9815.

[50] Hertel, E. *ZEITSCHRIFT FUR ELEKTROCHEMIE UND ANGEWANDTE PHYSIKALISCHE CHEMIE* **1931**, *37*, 536–538.

[51] Cohen, M. D.; Schmidt, G. M. J. *J. Chem. Soc.* **1964**, 1996–2000.

[52] Schmidt, G. M. J. *J. Chem. Soc.* **1964**, 2014–2021.

[53] Murthy, G.; Arjunan, P.; Venkatesan, K.; Ramamurthy, V. *Tetrahedron* **1987**, *43*, 1225–1240.

[54] Yue, Y.; Dai, J.; Jin, L.; Liu, C.; Sun, J.; Ye, K.; Lu, R. *Chemistry : A European Journal* **2023**, *29*, e202301525–n/a.

[55] Hayward, J. J.; Gumbau-Brisa, R.; Alberola, A.; Clarke, C. S.; Rawson, J. M.; Pilkington, M. *CrystEngComm* **2014**, *16*, 7268–7277.

[56] Gnanaguru, K.; Ramasubbu, N.; Venkatesan, K.; Ramamurthy, V. *Journal of Photochemistry* **1984**, *27*, 355–362.

[57] Nagarathinam, M.; Vittal, J. J. *Macromolecular Rapid Communications.* **2006**, *27*, 1091–1099.

[58] Gnanaguru, K.; Ramasubbu, N.; Venkatesan, K.; Ramamurthy, V. *Journal of Organic Chemistry* **1985**, *50*, 2337–2346.

[59] Murthy, G.; Arjunan, P.; Venkatesan, K.; Ramamurthy, V. *Tetrahedron* **1987**, *43*, 1225–1240.

[60] Yadava, K.; Vittal, J. J. *Crystal Growth & Design* **2019**, *19*, 2542–2547.

[61] Nakagawa, M.; Kusaka, S.; Kiyose, A.; Nakajo, T.; Iguchi, H.; Mizuno, M.; Matsuda, R. *Journal of the American Chemical Society* **2023**, *145*, 12059–12065.

[62] Peedikakkal, A. M. P. *Journal of Chemical Sciences (Bangalore, India)* **2017**, *129*, 733–739.

[63] Johnson, W. A.; Mehl, R. F. *Metallurgical and Materials Transactions. A, Physical Metallurgy and Materials Science* **2010**, *41A*, 2713–2775.

[64] Avrami, M. *The Journal of Chemical Physics* **1939**, *7*, 1103–1112.

[65] Avrami, M. *The Journal of Chemical Physics* **1940**, *8*, 212–224.

[66] Avrami, M. *The Journal of Chemical Physics* **1941**, *9*, 177–184.

[67] Fonseca, I.; Baias, M.; Hayes, S. E.; Pickard, C. J.; Bertmer, M. *Journal of Physical Chemistry. C* **2012**, *116*, 12212–12218.

[68] Benedict, J. B.; Coppens, P. *The Journal of Physical Chemistry. A, Molecules, Spectroscopy, Kinetics, Environment, & General Theory* **2009**, *113*, 3116–3120.

[69] Kumar, V.; Fusaro, L.; Aprile, C.; Robeyns, K.; Garcia, Y. *Crystal Growth & Design* **2020**, *20*, 7850–7861.

[70] Cao, D.-K.; Sreevidya, T. V.; Botoshansky, M.; Golden, G.; Brown Benedict, J.; Kaftory, M. *The Journal of Physical Chemistry. A, Molecules, spectroscopy, Kinetics, Environment, & General Theory* **2010**, *114*, 7377–7381.

[71] *Acta crystallographica. Section B, Structural Science* **2012**, *68*, 424–430.

[72] HANCOCK, J. D.; SHARP, J. H. *Journal of the American Ceramic Society* **1972**, *55*, 74–77.

[73] Christian, J. *The Theory of Transformations in Metals and Alloys: an advanced textbook in physical metallurgy*, 3rd ed.; Elsevier Science & Technology: London, 2002.

[74] Bentea, L.; Watzky, M. A.; Finke, R. G. *Journal of Physical Chemistry. C* **2017**, *121*, 5302–5312.

[75] Watzky, M. A.; Finke, R. G. *Journal of the American Chemical Society* **1997**, *119*, 10382–10400.

[76] Morris, A. M.; Watzky, M. A.; Agar, J. N.; Finke, R. G. *Biochemistry (Easton)* **2008**, *47*, 2413–2427.

[77] Tong, F.; Hanson, M. P.; Bardeen, C. J. *Physical Chemistry Chemical Physics : PCCP* **2016**, *18*, 31936–31945.

[78] Kaas, R. L. *Journal of polymer science. Polymer chemistry edition* **1981**, *19*, 2255–2267.

[79] Kohout, J. *Journal of Materials Science* **2008**, *43*, 1334–1339.

[80] Finney, E. E.; Finke, R. G. *Chemistry of Materials* **2009**, *21*, 4692–4705.

[81] Nakagawa, M.; Kusaka, S.; Kiyose, A.; Nakajo, T.; Iguchi, H.; Mizuno, M.; Matsuda, R. *Journal of the American Chemical Society* **2023**, *145*, 12059–12065.

[82] Chung, J. W.; You, Y.; Huh, H. S.; An, B.-K.; Yoon, S.-J.; Kim, S. H.; Lee, S. W.; Park, S. Y. *Journal of the American Chemical Society* **2009**, *131*, 8163–8172.

[83] Park, I.-H.; Chanthapally, A.; Zhang, Z.; Lee, S. S.; Zaworotko, M. J.; Vittal, J. J. *Angewandte Chemie (International ed.)* **2014**, *53*, 414–419.

[84] Raiser, D.; Sindlinger, C. P.; Schubert, H.; Wesemann, L. *Angewandte Chemie (International ed.)* **2020**, *59*, 3151–3155.

[85] Tan, Y. S.; Yeo, C. I.; Tiekink, E. R. T. *Crystal Growth & Design* **2024**, *24*, 3170–3178.

[86] Li, W.-X.; Gu, J.-H.; Li, H.-X.; Dai, M.; Young, D. J.; Li, H.-Y.; Lang, J.-P. *Inorganic chemistry* **2018**, *57*, 13453–13460.

[87] Khan, S.; Dutta, B.; Mir, M. H. *Dalton Transactions : an International Journal of Inorganic Chemistry* **2020**, *49*, 9556–9563.

[88] Friščić, T.; MacGillivray, L. R. *Zeitschrift für Kristallographie. Crystalline materials* **2005**, *220*, 351–363.

[89] Huang, S.-L.; Hor, T. A.; Jin, G.-X. *Coordination Chemistry Reviews* **2017**, *346*, 112–122.

[90] Kim, S.; An, J.; Choi, H.; Jung, S. H.; Lee, S. S.; Park, I.-H. *Inorganic chemistry* **2023**, *62*, 13173–13178.

[91] Rath, B. B.; Vittal, J. J. *Journal of the American Chemical Society* **2020**, *142*, 20117–20123.

[92] Khan, S.; Akhtaruzzaman,; Medishetty, R.; Ekka, A.; Mir, M. H. *Chemistry, an Asian journal* **2021**, *16*, 2806–2816.

[93] Khan, S.; Dutta, B.; Naaz, S.; Choudhury, A.; Cazade, P. A.; Kiely, E.; Guerin, S.; Medishetty, R.; Mir, M. H. *Communications Chemistry* **2023**, *6*, 150–150.

[94] Mittapalli, S.; Sravanakumar Perumalla, D.; Nangia, A. *IUCrJ* **2017**, *4*, 243–250.

[95] Canevet, D.; Sallé, M.; Zhang, G.; Zhang, D.; Zhu, D. *Chemical Communications (Cambridge, England)* **2009**, 2245–2269.

[96] Su, J.; Yuan, S.; Wang, H. Y.; Huang, L.; Ge, J. Y.; Joseph, E.; Qin, J.; Cagin, T.; Zuo, J. L.; Zhou, H. C. *Nature Communications* **2017**, *8*, 2008–8.

[97] Kreitsberga, Y.; Liepin'sh, E.; Mazheika, I.; Neiland, O. *J. Org. Chem. USSR (Engl. Transl.); (United States)* **1986**, *22:2*.

[98] Devic, T.; Batail, P.; Avarvari, N. *Chemical Communications (Cambridge, England)* **2004**, *1538*, 1538–1539.

[99] Jeannin, O.; Fourmigué, M. *Chemistry : A European Journal* **2006**, *12*, 2994–3005.

[100] Simao, C.; Mas-Torrent, M.; André, V.; Duarte, M. T.; Veciana, J.; Rovira, C. *Chemical science (Cambridge)* **2013**, *4*, 307–310.

[101] Simao, C.; Mas-Torrent, M.; André, V.; Teresa Duarte, M.; Techert, S.; Veciana, J.; Rovira, C. *CrystEngComm* **2013**, *15*, 9878–9884.

[102] Strauss, I.; Mundstock, A.; Treger, M.; Lange, K.; Hwang, S.; Chmelik, C.; Rusch, P.; Bigall, N. C.; Pichler, T.; Shiozawa, H.; Caro, J. *ACS Applied Materials & Interfaces* **2019**, *11*, 14175–14181.

[103] Wang, H.; Ge, J.; Hua, C.; Jiao, C.; Wu, Y.; Leong, C. F.; D'Alessandro, D. M.; Liu, T.; Zuo, J. *Angewandte Chemie (International ed.)* **2017**, *56*, 5465–5470.

[104] Souto, M.; Romero, J.; Calbo, J.; Vitorica-Yrezabal, I. J.; Zafra, J. L.; Casado, J.; Orti, E.; Walsh, A.; Minguez Espallargas, G. *Journal of the American Chemical Society* **2018**, *140*, 10562–10569.

[105] Wang, F.; Wang, J.; Maehrlein, S. F.; Ma, Y.; Liu, F.; Zhu, X.-Y. *The Journal of Physical Chemistry Letters* **2020**, *11*, 762–766.

[106] Su, J.; Xu, N.; Murase, R.; Yang, Z.; D'Alessandro, D. M.; Zuo, J.; Zhu, J. *Angewandte Chemie (International ed.)* **2021**, *60*, 4789–4795.

[107] Park, S. S.; Hontz, E. R.; Sun, L.; Hendon, C. H.; Walsh, A.; Van Voorhis, T.; Dinca, M. *Journal of the American Chemical Society* **2015**, *137*, 1774–1777.

[108] Alhamami, M.; Doan, H.; Cheng, C. H. *Materials* **2014**, *7*, 3198–3250.

[109] Kearns, E. R.; Clegg, J. K.; Lewis, W.; Fang, A.; Chan, B.; D'Alessandro, D. M. *Chemistry of Materials* **2022**, *34*, 10495–10500.

[110] Kearns, E. R.; D'Alessandro, D. M. *Crystal Growth & Design* **2023**, *23*, 6100–6106.

[111] Hall, L. Investigating Redox Activity and Structural Switching in Tetrathiafulvalene-Based Metal–Organic Frameworks. 2020.

[112] Dolomanov, O. V.; Bourhis, L. J.; Gildea, R. J.; Howard, J. A. K.; Puschmann, H. *Journal of Applied Crystallography* **2009**, *42*, 339–341.

[113] Sheldrick, G. M. *Acta Crystallographica. Section A, Foundations and Advances* **2015**, *71*, 3–8.

[114] Sheldrick, G. M. *Acta Crystallographica. Section C, Crystal Structure Communications* **2015**, *71*, 3–8.

[115] Scherrer, P. *Nachr. Ges. Wiss. Göttingen* **1918**, 96–100.

[116] Miranda, M. A. R.; Sasaki, J. M. *Acta Crystallographica. Section A, Foundations and Advances* **2018**, *74*, 54–65.

[117] Langford, J. I.; Wilson, A. J. C. *Journal of Applied Crystallography* **1978**, *11*, 102–113.

[118] He, K.; Chen, N.; Wang, C.; Wei, L.; Chen, J. *Crystal Research and Technology (1979)* **2018**, *53*, 1700157.

[119] Sangeetha Margreat, S.; Ramalingam, S.; Sebastian, S.; Xavier, S.; Periandy, S.; Daniel, J. C.; Maria Julie, M. *Journal of Molecular Structure* **2020**, *1200*, 127099.

[120] Park, I.; Lee, E.; Lee, S. S.; Vittal, J. J. *Angewandte Chemie (International ed.)* **2019**, *58*, 14860–14864.

Appendix

Table S.1: Full Factorial Optimisation weights for Zn-Pad Synthesis; Stoichiometric ratio is [Py_2TTF]:[$Zn_2(NO_3)_2 \cdot 6H_2O$]:H_2TDC, where 1 unit = 0.0188 mmol

Label	Time (h)	Temperature °C	Stoichiometry	FWHM of the 8.34° peak
i	24	80	2:2:2	0.07988
d	24	90	2:2:2	0.07046
dd	24	100	2:2:2	0.08899
a	48	80	2:2:2	0.06510
ad	48	90	2:2:2	0.08130
add	48	100	2:2:2	0.07377
b	24	80	1:2:2	0.1442
bd	24	90	1:2:2	0.10805
bdd	24	100	1:2:2	0.1560
ab	48	80	1:2:2	0.1700
abd	48	90	1:2:2	0.1150
abdd	48	100	1:2:2	0.1488

Table S.2: Full Factorial Optimisation weights for Zn-TDC Synthesis

Label	Time (h)	Temperature °C	Amount (mmol)	FWHM of the 8.34° peak
i	24	80	0.0377	0.07988
d	24	90	0.0377	0.07046
dd	24	100	0.0377	0.08899
a	48	80	0.0377	0.06510
ad	48	90	0.0377	0.08130
add	48	100	0.0377	0.07377
c	24	80	0.0188	0.06936
cd	24	90	0.0188	0.07776
cdd	24	100	0.0188	0.07775
ac	48	80	0.0188	0.09831
acd	48	90	0.0188	0.06813
acdd	48	100	0.0188	0.05216

Table S.3: Data collection for Zn-TDC

	Zn-TDC
Empirical Formula	$C_{48}H_{36}N_4O_{10}S_{10}Zn_2$
Formula Weight	1280.15
Collection Temperature (K)	100(2)
Wavelength (Å)	0.71073
Crystal System	Orthorhombic
Space Group	Pcca
a (Å)	17.763(4)
b (Å)	18.906(4)
c (Å)	16.404(3)
α (Å)	90
β (Å)	90
γ (Å)	90
Volume (Å^3)	5508.9(19)
Z	4
μ (mm^{-1})	1.308
F(000)	2608.0
Crystal Size (mm)	? ? ?
Theta range (°)	2.154 - 50.288
Reflections measured	31057
Independent reflections	9496
Data/restraints/parameters	9496/517/614
Goodness-of-fit on F^2	1.024
Final R indexes [I>=2σ (I)]	R_1 = 0.0840, wR_2 = 0.2223
Final R indexes [all data]	R_1 = 0.1147, wR_2 = 0.2451
Largest diff. peak/hole (Å^{-3})	1.40/-0.57
Flack parameter	0.10(3)

Table S.4: Data collection for Zn-Cyc

	Zn-Cyc
Empirical Formula	$C_{50}H_{38}N_6O_{10}S_{10}Zn_2$
Formula Weight	1334.20
Collection Temperature (K)	100.00(10)
Wavelength (Å)	1.54184
Crystal System	Orthorhombic
Space Group	Pcca
a (Å)	18.4987(11)
b (Å)	18.735(2)
c (Å)	15.7143(9)
α (Å)	90
β (Å)	90
γ (Å)	90
Volume (Å^3)	5446.3(8)
Z	4
μ (mm^{-1})	5.206
F(000)	2720.0
Crystal Size (mm)	0.14 0.1 0.02
2 Theta range (°)	8.764 - 144.12
Reflections measured	31902
Independent reflections	5215
Data/restraints/parameters	5215/1078/505
Goodness-of-fit on F^2	1.560
Final R indexes [I>=2σ (I)]	R_1 = 0.1559, wR_2 = 0.4376
Final R indexes [all data]	R_1 = 0.2038, wR_2 = 0.4635
Largest diff. peak/hole (Å^{-3})	2.15/-0.60

Table S.5: Data collection for Zn-Pad

	Zn-Pad
Empirical Formula	$C_{28}H_{14}N_2O_8S_6Zn_2$
Formula Weight	829.51
Collection Temperature (K)	100.0(2)
Wavelength (Å)	0.71073
Crystal System	Monoclinic
Space Group	$P2_1/c$
a (Å)	20.939(4)
b (Å)	15.101(3)
c (Å)	13.802(3)
α (Å)	90
β (Å)	102.45(3)
γ (Å)	90
Volume ($Å^3$)	4261.6(16)
Z	4
μ (mm^{-1})	1.459
F(000)	1664.0
Crystal Size (mm)	? ? ?
Theta range (°)	1.992 - 58.62
Reflections measured	9130
Independent reflections	9130
Data/restraints/parameters	9130/0/416
Goodness-of-fit on F^2	1.090
Final R indexes [I>=2σ (I)]	R_1 = 0.0885, wR_2 = 0.2663
Final R indexes [all data]	R_1 = 0.1286, wR_2 = 0.3070
Largest diff. peak/hole ($Å^{-3}$)	1.49/-1.18

Derivation of FW rate law for $[B]_0 \neq 0$

$$-\frac{d[A]}{dt} = \frac{d[B]}{dt} = k_1[A] + k_2[A][B]$$

Let $[A] + [B] = [A]_0 + [B]_0$

$$-\frac{d[A]}{dt} = k_1[A] + k_2[A]([A]_0 + [B]_0 - [A])$$

Let $k_1 + k_2[A]_0 + k_2[B]_0 = a$ and $-k_2 = b$

$$\begin{aligned} -\frac{d[A]}{dt} &= a[A] + b[A]^2 \\ \int_0^t dt &= \int_{[A]_0}^{[A]_t} \frac{-d[A]}{a[A] + b[A]^2} \\ &= -\int_{[A]_0}^{[A]_t} \frac{d[A]}{(\frac{a}{2\sqrt{b}} + \sqrt{b}[A])^2 - \frac{a^2}{4b}} \end{aligned}$$

Substitute $c = \frac{a}{2\sqrt{b}} + \sqrt{b}[A]$ and $dc = \sqrt{b}d[A]$

$$
\begin{aligned}
&= -\frac{1}{\sqrt{b}} \int_{[A]_0}^{[A]_t} \frac{1}{c^2 - \frac{a^2}{4b}} dc \\
&= -\frac{1}{\sqrt{b}} \int_{[A]_0}^{[A]_t} \frac{-4b}{a^2(-\frac{4bc^2}{a^2} + 1)} dc \\
&= \frac{4\sqrt{b}}{a^2} \int_{[A]_0}^{[A]_t} \frac{1}{-\frac{4bc^2}{a^2} + 1} dc
\end{aligned}
$$

Substitute $f^2 = \frac{-4bc^2}{a^2}$ and $f = \frac{2i\sqrt{b}c}{a}$ and $df = \frac{2i\sqrt{b}}{a} dc$

$$
\begin{aligned}
&= \frac{4\sqrt{b}}{a^2} \int_{[A]_0}^{[A]_t} \frac{1}{f^2 + 1} \frac{a}{2i\sqrt{b}} df \\
&= -\frac{2i}{a} \int_{[A]_0}^{[A]_t} \frac{1}{f^2 + 1} df \\
&= \left[-\frac{2i}{a} tan^{-1}(f) \right]_{[A]_0}^{[A]_t} \\
&= \left[-\frac{2i}{a} tan^{-1}(\frac{2i\sqrt{b}c}{a}) \right]_{[A]_0}^{[A]_t}
\end{aligned}
$$

Use the property $tanh^{-1}(x) = \frac{1}{i} tan^{-1}(ix)$

$$
\begin{aligned}
&= \left[\frac{2}{a} tanh^{-1}(\frac{2\sqrt{b}c}{a}) \right]_{[A]_0}^{[A]_t} \\
&= \left[\frac{2}{a} tanh^{-1}(\frac{2\sqrt{b}}{a}(\frac{a}{2\sqrt{b}} + \sqrt{b}[A])) \right]_{[A]_0}^{[A]_t} \\
&= \left[\frac{2}{a} tanh^{-1}(1 + \frac{2b}{a}[A]) \right]_{[A]_0}^{[A]_t}
\end{aligned}
$$

Use the property $tanh^{-1}(x) = \frac{1}{2}(ln(1+x) - ln(1-x))$

$$= \left[\frac{1}{a}(ln(\frac{a+b[A]}{[A]})\right]_{[A]_0}^{[A]_t}$$
$$t = \left[(ln(\frac{a+b[A]}{[A]})\right]_{[A]_0}^{[A]_t}$$
$$at = ln(\frac{a+b[A]_t}{[A]_t}) - ln(\frac{a+b[A]_0}{[A]_0})$$
$$at = ln(\frac{a+b[A]_t}{[A]_t}\frac{[A]_0}{a+b[A]_0})$$
$$e^{at} = \frac{a[A]_0 + b[A]_t[A]_0}{(a+b[A]_0)[A]_t}$$

Substitute $a = k_1 + k_2[A]_0 + k_2[B]_0$

$$e^{(k_1+k_2[A]_0+k_2[B]_0)t} = \frac{(k_1 + k_2[A]_0 + k_2[B]_0)[A]_0 + b[A]_t[A]_0}{(k_1 + k_2[A]_0 + k_2[B]_0 + b[A]_0)[A]_t}$$

Substitute $b = -k_2$

$$e^{(k_1+k_2[A]_0+k_2[B]_0)t} = \frac{(k_1 + k_2[A]_0 + k_2[B]_0)[A]_0 - k_2[A]_t[A]_0}{(k_1 + k_2[B]_0)[A]_t}$$

$$(\frac{k_1}{k_2} + [B]_0)e^{(k_1+k_2[A]_0+k_2[B]_0)t} =$$
$$(\frac{k_1}{k_2} + [B]_0)\frac{(k_1 + k_2[A]_0 + k_2[B]_0)[A]_0}{(k_1 + k_2[B]_0)[A]_t} - (\frac{k_1}{k_2} + [B]_0)\frac{k_2[A]_t[A]_0}{(k_1 + k_2[B]_0)[A]_t}$$

$$(\frac{k_1}{k_2} + [B]_0)e^{(k_1+k_2[A]_0+k_2[B]_0)t} = \frac{k_1 + k_2[B]_0}{k_2}\frac{(k_1 + k_2[A]_0 + k_2[B]_0)[A]_0}{(k_1 + k_2[B]_0)[A]_t} - [A]_0$$
$$k_2[A]_0 + (k_1 + k_2[B]_0)e^{(k_1+k_2[A]_0+k_2[B]_0)t} = \frac{(k_1 + k_2[A]_0 + k_2[B]_0)[A]_0}{[A]_t}$$
$$[A]_t = \frac{(k_1 + k_2[A]_0 + k_2[B]_0)[A]_0}{k_2[A]_0 + (k_1 + k_2[B]_0)e^{(k_1+k_2[A]_0+k_2[B]_0)t}}$$
$$[A]_t = \frac{\frac{k_1}{k_2} + [A]_0 + [B]_0}{1 + (\frac{k_1}{k_2[A]_0} + \frac{[B]_0}{[A]_0})e^{(k_1+k_2[A]_0+k_2[B]_0)t}}$$

(a) (b) (c)

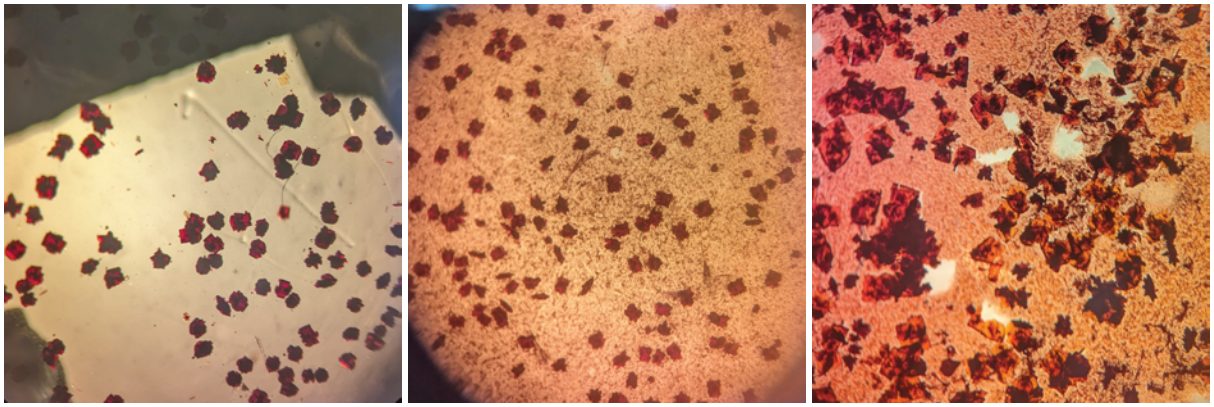

(d) (e) (f)

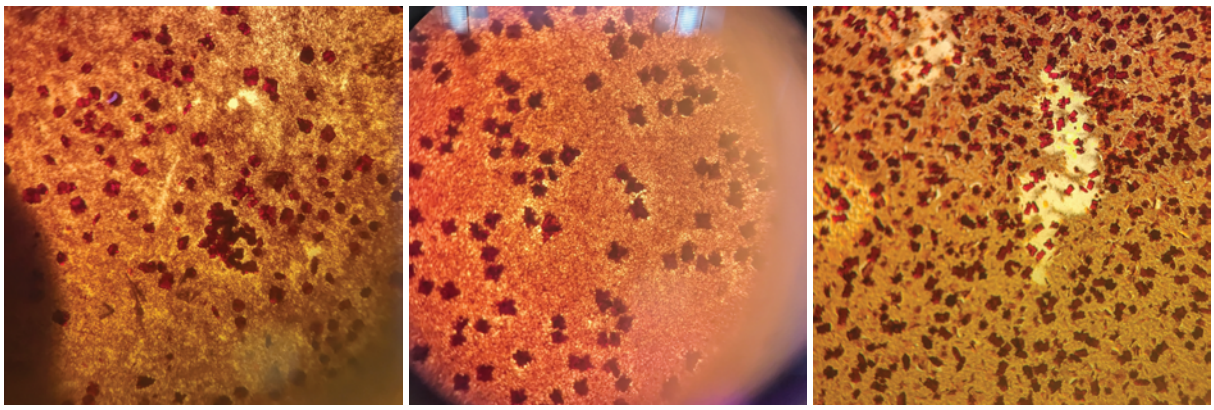

(g) (h) (i)

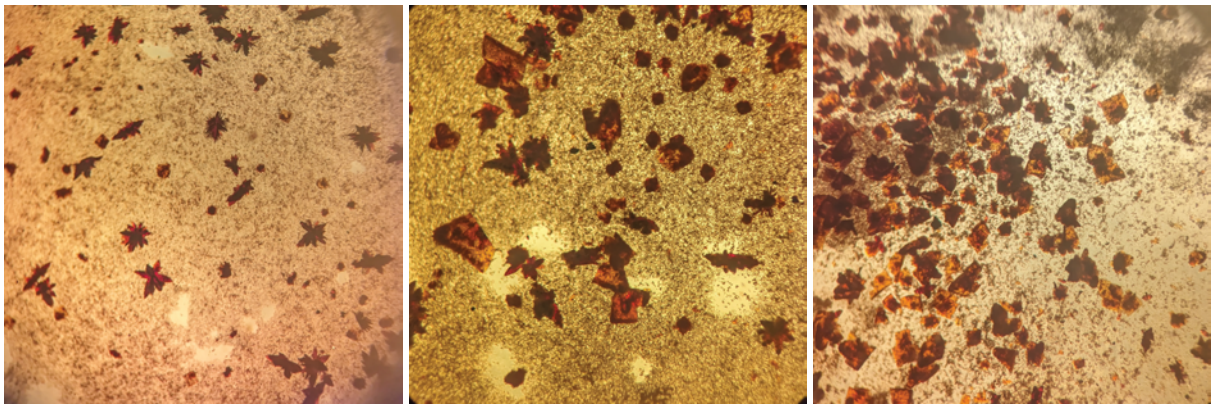

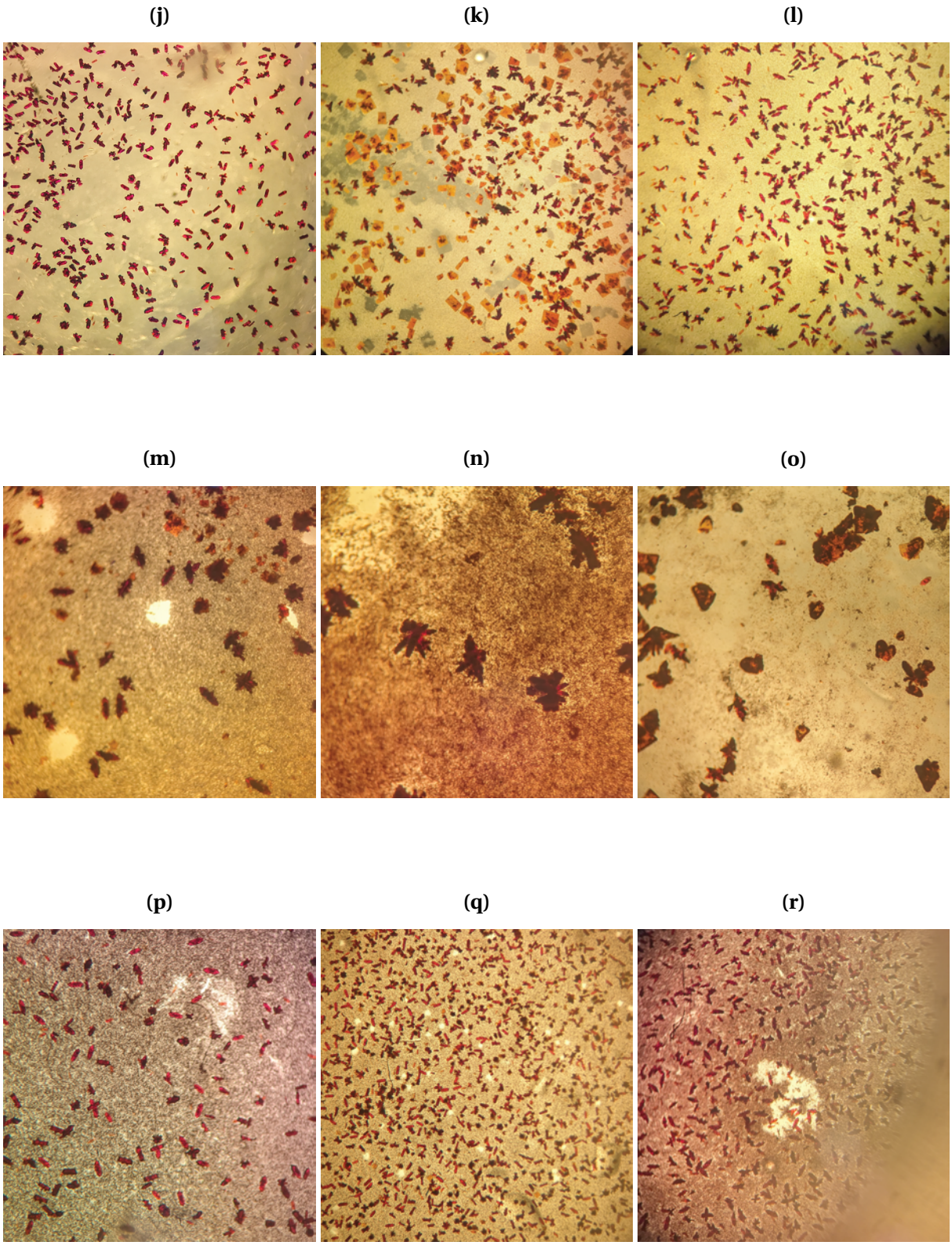

Figure S.1: Solvothermal results from the corresponding synthetic conditions (a) i, (b) d, (c) dd, (d) a, (e) ad, (f) add,(g) b, (h) bd, (i) bdd, (j) c, (k) cd, (l) cdd, (m) ab, (n) abd, (o) abdd, (p) ac, (q) acd, (r) acdd